Economic Geology
Vol. 75, 1980, pp. 384–409

Deep Hypogene Oxidation of Porphyry Copper Potassium-Silicate Protore at Butte, Montana: A Theoretical Evaluation of the Copper Remobilization Hypothesis

GEORGE H BRIMHALL, JR.

Abstract

The oxidation effects of potassium-silicate protores from heated meteoric water have been thermodynamically computed and confirm previously described copper vein-forming mechanisms involving hypogene leaching and enrichment of chalcopyrite-bearing protore (Brimhall, 1979). Intense copper leaching of protore chalcopyrite is shown to be related to a state of peroxidation in which the only stable minerals are quartz, pyrite, and muscovite following the complete destruction of the wall-rock oxygen fugacity buffer assemblage including hematite dissolution. Because modification of the protore continues to higher fluid/rock ratios, copper is extracted from the fluid phase and again is fixed in the rock as sulfides, first as bornite and ultimately as chalcocite-covellite associated with the advanced argillic alteration assemblage. This end-stage assemblage should occur only where extremely high fluid/rock ratios are reached in zones of unusually high permeability near the source of the heat responsible for the fluid motion.

The results of the calculations are interpreted to mean that certain intervals of fluid/rock ratio are characterized by net base metal leaching and other intervals by metal fixation. Attainment of only intermediate fluid/rock ratios may result in the major amount of the copper in a protore being remobilized into solution and leaving the system through ground-water circulation. In contrast, in highly evolved systems where the fluid/rock ratio has increased to extremely high values, the presence of an advanced argillic alteration assemblage with chalcocite and covellite strongly suggests the presence within a district of a partially oxidized, potassium-silicate, disseminated sulfide protore, including a strongly leached and sericitized quartz-pyrite protore relict.

Near-surface vein mineralization may conceivably be related to primary or unoxidized protore at depth in two distinct ways, depending upon the origin of the intrusives and the fracture systems responsible for circulation of oxidizing meteoric water. First, late intrusives which are cogenetic with the magmatic heat source of the protore may remobilize ore-forming elements upon deep hypogene oxidation of pyritic disseminated sulfides. Second, much later, totally unrelated intrusive activity and deep crustal faulting, perhaps related to entirely different petrotectonic regimes, may provide access for meteoric water to penetrate much older protores, resulting in the formation of near-surface ore deposits by element recycling.

It is therefore suggested that near-surface hydrothermal base and precious metal deposits be explored to considerable depths for possible low-grade protore potential.

Introduction

IT has been demonstrated lithologically that large, high-grade, copper-zinc vein systems at Butte, Montana, are probably the result of hydrothermal remobilization of base metals originally deposited in a porphyry copper potassium-silicate protore (Brimhall, 1978, 1979). Analysis of the whole-rock copper content as a function of the level of late-stage protore modification has shown that progressive interaction of magmatically heated meteoric water with highly fractured protore is responsible for intense chalcopyrite-sphalerite leaching, followed in most of the western third of the district by pyrite and ultimately Cu-Fe-As sulfide deposition in the high-grade veins. A genetic link has therefore been clearly established between early, high-temperature protore mineralization and later, low-temperature vein formation in which the fluid circulation within the vein systems is probably driven by a relatively young, high-level intrusive complex in the central part of the Butte district (Modoc dike system near the Leonard mine, Fig. 1). Although the chemical mass transfer mechanisms of vein formation have been shown to involve hypogene leaching and subsequent hypogene enrichment of low-grade protore material—eliminating the problematical necessity of a late-stage magmatic metal source for at least some of the ore-forming elements—the physical and thermodynamic controls on the entire nonequi-

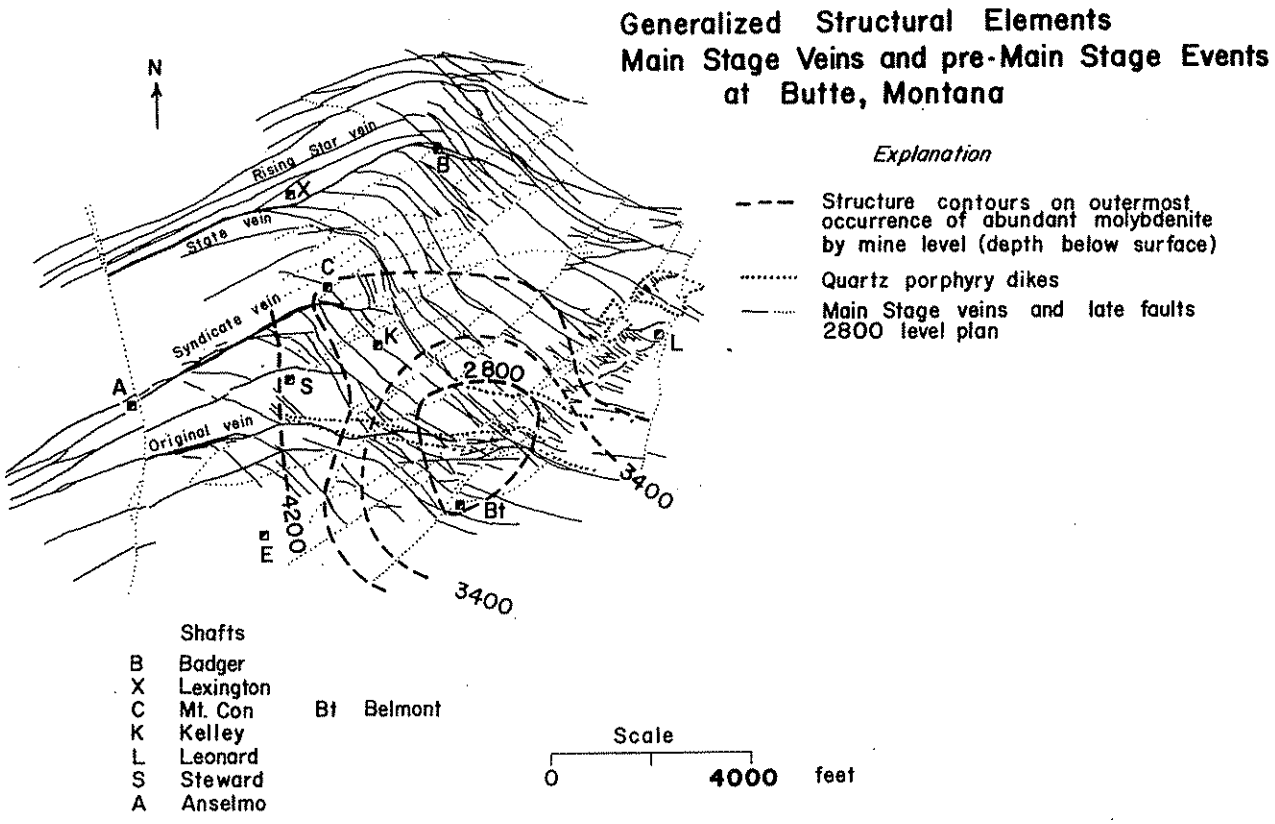

FIG. 1. Plan map of the Butte district, Montana, showing the locus of pre-Main Stage (protore) occurrences of abundant molybdenite by structure contours given by mine level, approximately equal to the distance below the surface (Meyer et al., 1968). Related to the 62-m.y.-old protore are east-west-striking Steward quartz porphyry dikes. Later Main Stage Butte veins (57–59 m.y. old) are shown in plan on the 2800 level, overlapping the protore molybdenite dome in a circular area just north of the Belmont shaft. A relatively young quartz porphyry intrusive complex in the Leonard mine area (Modoc system) may be related to vein formation and to the advanced argillic alteration assemblage.

librium process of element recycling have not yet been quantitatively investigated. The present study attempts to isolate the most important geological and geochemical factors responsible for postdepositional element mobility, including sulfide leaching and reprecipitation controls in alteration assemblages of progressively higher levels of hydrolytic attack.

Although isotope geochemistry has offered much insight into the origins of water, rocks, and sulfur in hydrothermal ore deposits, relatively little is known about the processes by which metals ultimately attain ore-grade concentration levels in hypogene environments. There is, however, much speculation about the reconcentration of metals and upgrading of rock masses, which, considered on a crustal basis, have anomalous metal contents. Conceptually, it would seem to be a simple matter to determine the extent to which metals have been remobilized. In practice, however, the enormous physical dimensions of the magmatic-hydrothermal systems involved, as well as economic constraints on exploration and mine development, preclude all but the most cursory examination of this problem using district-scale geometrical mass balance constraints. There are, fortunately, other viable means to address the problem of repetitive metal concentration, i.e., those outlined earlier by Graton and Bowditch (1936), Lacy and Hosmer (1956), and Lowell (1974); the lithologic approach used in Brimhall (1979); and the chemical thermodynamic analysis offered in this study.

In the model proposed, the near-vein sericitic alteration facies is one in which the copper-bearing protore sulfide, chalcopyrite, is progressively leached, yielding copper, iron, and sulfur to the infiltrating, strongly acid, vein fluid. The intensity of sericitization of K-silicate protore seems to affect the relative level of disseminated chalcopyrite destruction. It is reasoned that fluids responsible for the most intense wall-rock alter-

ation are also capable of the strongest copper leaching and represent, therefore, one end of a spectrum of hydrothermal ore-forming fluids, the end most distinctly different from the protore assemblage and most characteristic of the vein environment.

Phase equilibria studies indicate that sulfide assemblages occurring in the most intensely altered and fractured wall rocks have formed from fluids with relatively high oxygen and sulfur fugacities (Meyer and Hemley, 1967). This alteration environment, the so-called advanced argillic assemblages, characterized by extreme base leaching and hydrogen ion metasomatism of wall rocks, often contains the assemblage alunite-muscovite-kaolinite (or pyrophyllite)-quartz (Hemley et al., 1969), accompanied by covellite-pyrite and covellite-chalcocite in a dense microfracture or "horsetail" veinlet system (Meyer et al., 1968) as well as in the veinward edge of the sericitic alteration facies. The water composition responsible for this advanced argillic assemblage represents a meteoric hydrothermal stage with the most highly ^{18}O-depleted character of the Butte ore-forming fluids (Sheppard and Taylor, 1974). It is likely, then, that these fluids are most representative of the vein ore-forming solutions. However, it is necessary to keep in mind that these meteoric fluids have compositions which have evolved somewhat by reaction with their wall rocks over the continuous pressure-temperature path of convection about the heat source. This study deals only with isobaric-isothermal reactions of the advanced argillic fluid with K-silicate protore and leaves for another future study the means by which the oxidizing fluid attains its chemical composition during migration through pyritic protore wall rock.

The purpose of the present study is only to test the thermodynamic feasibility of the element-recycling hypothesis by computing, using irreversible thermodynamics (Helgeson, 1968, 1971; Helgeson et al., 1969, 1970; Wolery, 1979), the effects of interacting K-silicate protore assemblages with strongly oxidizing aqueous fluids compatible with the advanced argillic alteration assemblage. If the hypothesis is in fact correct, then path-dependent thermodynamic predictions of progressively changing mineral assemblages and associated copper-content variation should closely approximate the available geological data (Brimhall, 1979), including copper leaching. The mineralogic and assay data base necessary to constrain realistically such theoretical calculations has been established at this time in only a very few mining districts. It is hoped that conclusions regarding the genesis of the Butte deposit are of general application and will be tested by further study in other porphyry copper districts. Additionally, it is hoped that by determining the geological nature of the necessary and sufficient conditions for high-grade vein formation from fracture-controlled disseminated sulfide protores, exploration geologists will be more able to determine the likelihood of deep, large tonnage, low-grade protores underlying surficial base or precious metal vein exposures.

The success rate of deep exploration may substantially be improved when a clear understanding is attained of the configuration and spatial relationships of individual ore types within given magmatic-hydrothermal systems. A corollary of the element recycling hypothesis is that net depletion zones exist within the zoning pattern of vein deposits, representing leached protore relicts. It is vital to successful mineral exploration, therefore, to recognize and understand the geological significance of these low-grade, but genetically important, zones.

Previous Work

Numerous geological studies have offered direct evidence concerning the nature of near-surface oxidation of sulfide ores (e.g., Anderson, 1955; Titley, 1978). Although the upper crust of the earth is known to be a zone of active mixing of oxygenated meteoric water and deep-seated magmatic rocks and fluids (e.g., Taylor, 1974), the effects of deep oxidation of sulfide ores are, however, relatively unknown. The highly fractured mineralized rocks in porphyry copper deposits are especially interesting in this regard as they have been affected by unusually large quantities of reactive aqueous fluids driven by convective overturn within the thermal influence of cooling plutons and dike systems (Taylor, 1974; Sheppard and Taylor, 1974; Norton and Knight, 1977). These complex deposits are usually but not invariably characterized by the early dominance of magmatic water which may be responsible for intense hydrofracturing of the wall rock (Burnham, 1967). Increasing proportions of meteoric water are found in late-stage alteration mineral assemblages (Taylor, 1974; Sheppard and Taylor, 1974; White, 1974), often obliterating the mineralogic and isotopic nature of the early protore. Nevertheless, evolutionary trends are discernible within individual porphyry deposits which are reflected in a complete spectrum of ore types, from K-silicate (Creasy, 1959; Meyer, 1965) protores formed at high temperatures (Brimhall, 1977), supposedly by magmatic water, to end-stage lode deposits with high alteration levels characteristic of much lower temperatures and strong hydrolytic

attack of wall rocks (Einaudi, 1977). Fortunately, certain common elements characterize the porphyry deposits. These systematics have been discussed in the literature and include a parallel evolution of host-rock intrusives, fracture systems, alteration types, and ore mineral assemblages (Lowell and Guilbert, 1970; Gustafson and Hunt, 1975; Hollister, 1978, 1979).

Two basically distinct petrochemical stock-work types exist, differing principally in the composition of the host rock plutons (Hollister, 1978). The Lowell and Guilbert model (1970) of porphyry copper deposits occurs invariably where a Precambrian cratonic crust may be inferred at depth and is associated with calc-alkalic plutons of the granodiorite-quartz monzonite range (Hollister, 1978). The diorite model of Hollister (1978), in contrast, applies to essentially quartz-free plutons that commonly contain only the potassic and propylitic mineral assemblages and lack the strong phyllic zone of the Lowell and Guilbert model (1970). The high gold content and low concentration of molybdenum in silica-poor porphyries of the diorite model are compatible with processes of ore formation which are relatively unaffected by sialic crustal contamination (Hollister, 1978). The petrologic differences of the two systems are further reflected in the primary sulfide-oxide silicate assemblages of the protores. The Lowell and Guilbert model includes potassium-silicate assemblages (biotite and orthoclase) with a deep central chalcopyrite-bornite assemblage, surrounded by a peripheral pyrite-chalcopyrite±magnetite assemblage (Gustafson and Hunt, 1975; Hollister, 1978; Brimhall, 1977, 1979). In contrast, the orthoclase-deficient diorite model has a deep central bornite-magnetite assemblage surrounded by a pyrrhotite-chalcopyrite assemblage (Hollister, 1978).

The detailed mineralogical nature of one of these protore types has been shown in a preliminary manner to influence the subsequent effects of deep hypogene leaching and enrichment (Brimhall, 1979) by heated meteoric fluids. The early chalcopyrite-pyrite-magnetite assemblage at Butte apparently provided an important buffering effect on the evolution of the oxidizing Main Stage fluids and, to a certain extent, determined the ultimate copper grade of the hypogene-enriched product consisting of high-grade veins in sericitized wall rock. Earlier treatments of the petrochemical constraints on postmagmatic hydrothermal evolution have discussed the "main line" sulfidation states during ore deposition (Holland, 1965; Barton, 1970), as well as the alteration silicate-buffering effects upon sulfide solubilities (Hemley et al., 1967; Meyer and Hemley, 1967) and the effects of redox reactions accompanying wall-rock alteration involving pyrite, pyrrhotite, magnetite, and hematite (Raymahashay and Holland, 1969). A major extension of the available phase equilibria is necessary, however, to describe biotite-orthoclase-bearing protore assemblages of various types and to determine quantitatively the chemical reaction paths attending oxidation of these protores by metal-charged meteoric water. This paper, accordingly, involves two related parts. The first part provides the mineralogical and geochemical framework in which to analyze the oxidation process and the second presents the reaction paths in coordinate systems appropriate to the deduction of geological controls on copper mobility at low to moderate temperatures. This effort is only a first attempt to assess the quantitative feasibility of the element recycling hypothesis. Future studies must, in addition to the rock and fluid compositions investigated here, analyze reaction paths covering the full range of pressure-temperature conditions appropriate to the convective system during an influx of barren meteoric water into pyritic protore masses. Furthermore, the role of magmatic gases and the source of arsenic must be critically assessed.

Mineral Stability Relationships

Stability fields of sulfides, oxides, and silicates in the various protore assemblages may be effectively shown by augmenting presently available sulfur-oxygen fugacity diagrams (Holland, 1959, 1965; Meyer and Hemley, 1967) to include biotite (annite) and orthoclase. In addition, the secondary minerals developed from these protore assemblages during low-temperature oxidation by meteoric fluids may also be depicted. Estimates of the temperatures attending late-stage fluid circulation at Butte have been made from fluid inclusion studies (Meyer et al., 1968) and indicate a range of 200° to 350°C, with the peripheral parts of the district not more than 50° cooler than the central portions. Phase relations have been calculated at a temperature of 300°C and 500 bars, representing conditions taken to be characteristic of Main Stage hydrothermal activity.

Calculated phase boundaries are shown in Figure 2 and were constructed using internally consistent thermodynamic data from the SUPCRIT program (Helgeson et al., 1974, 1978, 1980). Heavy solid lines separate the stability fields of covellite, chalcocite, pyrite, pyrrhotite, magnetite, and hematite. Equilibrium constants at 300°C and 500 bars, as well as the defining mineral-gas equilibria, are given in Table 1 (reactions 1–6). The standard nature of these reactions requires no further explanation. Several new aspects of the

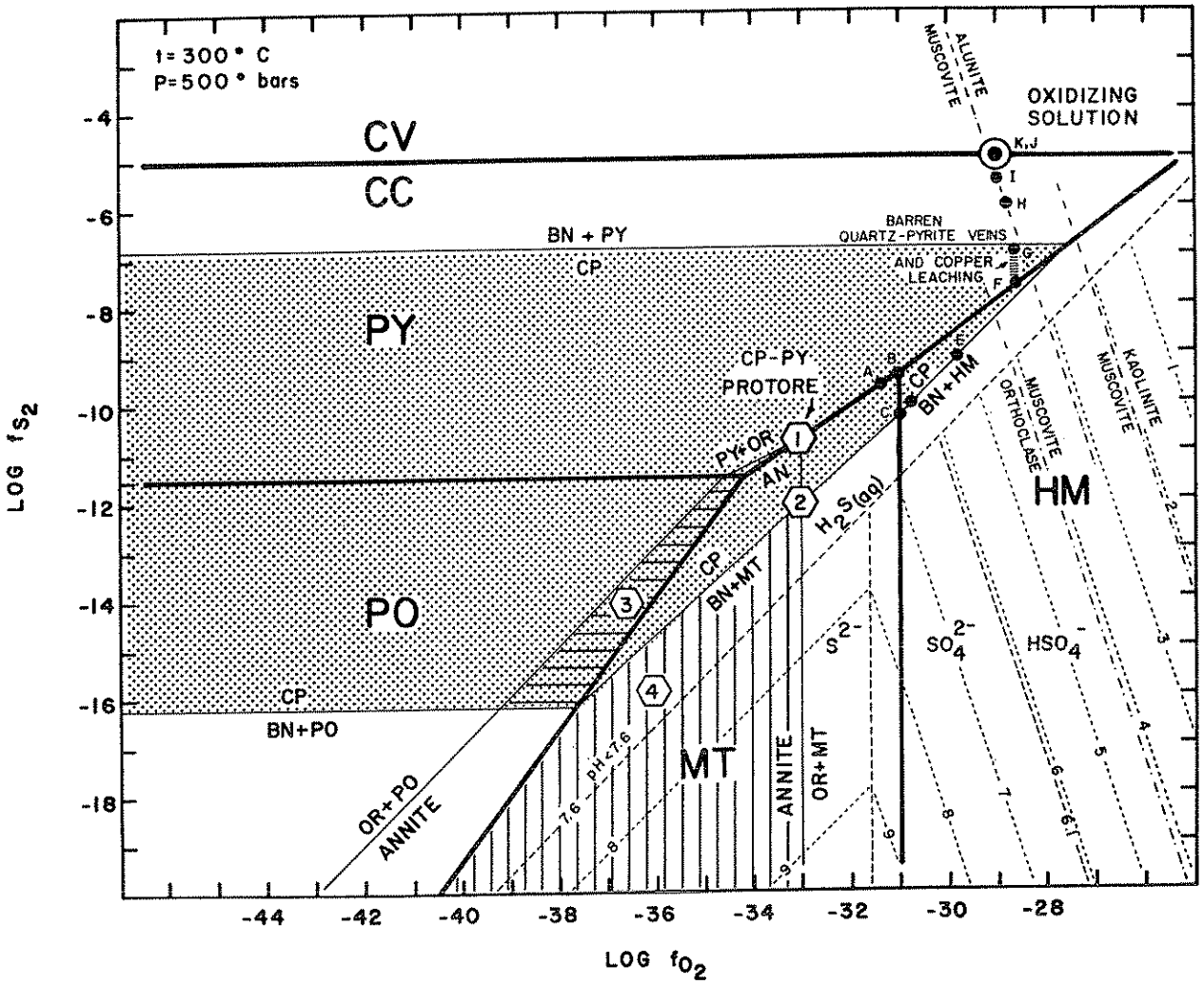

FIG. 2. Isothermal (300°C)-isobaric (500 bars) fugacity diagram showing the stability field of covellite (CV), chalcocite (CC), pyrite (PY), pyrrhotite (PO), magnetite (MT), and hematite (HM). The stability field of chalcopyrite (CP), bounded by bornite (BN) plus one other oxide or sulfide, is shown with a dotted pattern. In addition the stability field of annite (AN), bounded by orthoclase plus one other sulfide or oxide, is shown as a triangular area. Two types of porphyry copper protore from each of the porphyry models, i.e., Lowell and Guilbert (1970) and diorite (Hollister, 1978), are depicted on the basis of the minerals present and are shown as hexagons in the figure. The protores of the Lowell and Guilbert model (1970) are deep, Butte-type chalcopyrite-pyrite-biotite-orthoclase + magnetite assemblages (1). Deep core bornite-chalcopyrite-biotite-orthoclase + magnetite assemblages are designated by (2). Protores of the diorite model (Hollister, 1978) often lack orthoclase; consequently, the solution compositions are not as well constrained mineralogically, occurring within the annite field. The deep peripheral chalcopyrite-pyrrhotite-biotite (annite) assemblages are shown as (3) with a horizontal lined pattern; and deep core bornite-magnetite-biotite assemblages are designated by (4) shown with a vertical lined pattern. The composition of the oxidizing fluid compatible with the advanced argillic alteration assemblage is shown at the intersection of the covellite-chalcocite and alunite-muscovite phase boundaries. Aqueous sulfur speciation is shown by (long-dashed) boundaries of equal activity for a solution with total sulfur of 0.01 molal. Lines of constant pH are shown as short-dashed lines. Muscovite-orthoclase and kaolinite-muscovite phase boundaries are shown for a 1 molal KCl solution (Montoya and Hemley, 1975). The computed reaction path for the protore (1) is shown by letters A through K; see also Figures 7A, 12B, and 13. Notice that $H_2S_{(aq)}$ is the dominant sulfur species along the entire reaction path. Barren pyrite-quartz veins and intense copper leaching occur between F and G at maximum oxygen fugacity. Thermodynamic data is from Helgeson et al., 1974, 1978, 1980; see Table 1 for reactions.

phase equilibria depicted in Figure 2 do, however, require a more detailed discussion. The stability field of chalcopyrite is shown bounded by bornite. These equilibria are given in Table 1 (reactions 7–10) and involve bornite-chalcopyrite coexisting with pyrite (highest $\log f_{S_2}$), hematite (highest

TABLE 1. Equilibrium Constants Used in Phase Diagrams (computed using the SUPCRIT program of Helgeson et al., 1974, 1978, 1980)

Reaction no.	log K(t = 300°C, p = 500 bars)	
		Log f_{S_2} vs. log f_{O_2} (Fig. 2)
		Pyrite-pyrrhotite-magnetite-hematite-chalcopyrite-covellite fields
1	−27.6566	hematite + $2S_2$ = 2 pyrite + $1.5O_2$
2	33.7347	3 pyrite + $2O_2$ = magnetite + $3S_2$
3	5.75826	pyrrhotite + $0.5S_2$ = pyrite
4	15.5004	2 magnetite + $0.5O_2$ = 3 hematite
5	51.0095	3 pyrrhotite + $2O_2$ = magnetite + $1.5S_2$
6	−2.49972	2 covellite = chalcocite + $0.5S_2$
		Chalcopyrite field (Fig. 2)
7	−6.83103	bornite + 4 pyrite = 5 chalcopyrite + S_2
8	−62.1442	bornite + 2 hematite + $3S_2$ = 5 chalcopyrite + $3O_2$
9	−155.432	3 bornite + 4 magnetite + $9S_2$ = 15 chalcopyrite + $8O_2$
10	16.2020	bornite + 4 pyrrhotite + S_2 = 5 chalcopyrite
		Annite field (Fig. 2)
11	−34.5083	annite + $1.5S_2$ = orthoclase + 3 pyrrhotite + water + $1.5O_2$
12	−17.2335	annite + $3S_2$ = orthoclase + 3 pyrite + water + $1.5O_2$
13	16.5012	annite + $0.5O_2$ = orthoclase + water + magnetite
		Orthoclase-muscovite-kaolinite-alunite fields (Fig. 2)
14	−92.3143	alunite + 3 quartz = muscovite + S_2 + $3O_2$ + 2 water
15	−7.90771	muscovite + $2K^+$ + 6 quartz = 3 orthoclase + $2H^+$
16	7.58615	4 muscovite + $4H^+$ + 6 water = 6 kaolinite + $4K^+$
		Log ($a_{Fe^{+2}}/a^2_{H^+}$) vs. log (a_{Cu^+}/a_{H^+}) (Fig. 3)
17	−52.9652	2 bornite + Fe^{+2} + $8H^+$ + 4 water = magnetite + $10Cu^+$ + $8H_2S$
18	15.7455	magnetite + $2Cu^+$ + $4H_2S$ = 2 chalcopyrite + Fe^{+2} + 4 water
19	1.18041	magnetite + $2H^+$ = hematite + Fe^{+2} + water
20	5.00387	magnetite + $4H^+$ + $2H_2S$ = pyrite + $2Fe^{+2}$ + 4 water
21	14.5651	hematite + $2Cu^+$ + $4H_2S$ = 2 chalcopyrite + $2H^+$ + 3 water
22	3.82346	hematite + $2H^+$ + $2H_2S$ = pyrite + Fe^{+2} + 3 water
23	10.3190	hematite + $2H^+$ + $2H_2S$ + $2Cu^+$ = 2 covellite + 3 water + $2Fe^{+2}$
24	6.49553	pyrite + $2Cu^+$ = 2 covellite + Fe^{+2}
25	−23.9807	bornite + $6H^+$ = 0.5 pyrite + $5Cu^+$ + $0.5Fe^{+2}$ + $3H_2S$
26	10.7416	pyrite + $2Cu^+$ + Fe^{+2} + $2H_2S$ = 2 chalcopyrite + $4H^+$
27	18.6099	chalcopyrite + $4Cu^+$ + $2H_2S$ = bornite + $4H^+$
28	20.7329	covellite + $4Cu^+$ + Fe^{+2} + $3H_2S$ = bornite + $6H^+$
29	−51.7848	2 bornite + 3 water + $10H^+$ = $10Cu^+$ + $8H_2S$ + hematite
30	4.54210	annite + $6H^+$ = orthoclase + $3Fe^{+2}$ + 4 water
		Hydrolysis reactions
31	−5.35734	pyrite + water + $1.5H^+$ = Fe^{+2} + $1.75H_2S$ + $0.25SO_4^{-2}$
32	0.90602	pyrrhotite + $2H^+$ = Fe^{+2} + H_2S
33	−5.92644	covellite + 0.5 water + $0.75H^+$ = Cu^+ + $0.875H_2S$ + $0.125SO_4^{-2}$
34	−8.84805	chalcocite + $2H^+$ = $2Cu^+$ + H_2S
35	−8.04949	chalcopyrite + 0.5 water + $2.75H^+$ = Fe^{+2} + Cu^+ + $1.875H_2S$ + $0.125SO_4^{-2}$
36	−26.6593	bornite + 0.5 water + $6.75H^+$ = Fe^{+2} + $5Cu^+$ + $3.875H_2S$ + $0.125SO_4^{-2}$
37	−1.53388	hematite + $3.5H^+$ + $0.25H_2S$ = $2Fe^{+2}$ + $0.25SO_4^{-2}$ + 2 water
38	−0.35347	magnetite + $5.5H^+$ + $0.25H_2S$ = $3Fe^{+2}$ + $0.25SO_4^{-2}$ + 3 water
		Log ($a_{Fe^{+2}}/a^2_{Cu^+}$) vs. log $f_{H_2S(g)}$ (Fig. 4)
39	−28.8434	bornite + 2 hematite + $2.5Fe^{+2}$ + 4 water = 2.5 magnetite + $5Cu^+$ + $4H_2S$
40	−17.7255	0.5 bornite + 1.25 pyrite + $1.25Fe^{+2}$ + 4.5 water = 1.5 hematite + $2.5Cu^+$ + $4.5H_2S$
41	−7.87276	chalcopyrite + $0.5Fe^{+2}$ + 2 water = 0.5 magnetite + Cu^+ + $2H_2S$
42	−18.3886	pyrite + 2 chalcopyrite + Fe^{+2} + 6 water = 2 hematite + $2Cu^+$ + $6H_2S$
43	−7.86821	bornite + pyrite + Fe^{+2} = 3 chalcopyrite + $2Cu^+$
44	−3.24777	covellite + $0.5Fe^{+2}$ = 0.5 pyrite + Cu^+
45	−25.8449	0.5 bornite + 2.5 covellite + $2.5Fe^{+2}$ + 4.5 water = 1.5 hematite + $5Cu^+$ + $4.5H_2S$
46	−10.5204	5 chalcopyrite + 6 water = bornite + 2 hematite + $6H_2S$

TABLE 1.—(*Continued*)

Reaction no.	log K(t = 300°C, p = 500 bars)	
47	−5.81123	3 chalcocite + covellite + Fe^{+2} = bornite + 2 Cu^{+}
48	1.32153	hematite + H_2S = 0.5 pyrite + 0.5 magnetite + water
49	56.5893	magnetite + 4 pyrrhotite + 10Cu^{+} + 4H_2S = 2 bornite + 5Fe^{+2} + 4 water
50	3.19183	magnetite + 4H_2S = pyrite + 2 pyrrhotite + 4 water
51	12.5537	pyrite + 2 pyrrhotite + 2Cu^{+} = 2 chalcopyrite + Fe^{+2}
52	20.4219	chalcopyrite + 2 pyrrhotite + 4Cu^{+} = bornite + 2Fe^{+2}
53	−17.5730	2 bornite + Fe^{+2} + 4 water = magnetite + 4 chalcocite + 2Cu^{+} + 4H_2S
54	−9.7541	chalcocite + Fe^{+2} = pyrrhotite + 2Cu^{+}
		Oxygen-sulfate exchange reaction
55	46.4227	$H_2S + 2O_2 = 2H^{+} + SO_4^{-2}$
		Oxidation reactions
56	−16.9630	pyrite + water + 2H^{+} = Fe^{+2} + 2H_2S + 0.5O_2
57	−11.7293	covellite + 0.5 water + H^{+} = Cu^{+} + H_2S + 0.25O_2
58	−13.8523	chalcopyrite + 0.5 water + 3H^{+} = Fe^{+2} + Cu^{+} + 2H_2S + 0.25O_2
59	−32.4622	bornite + 0.5 water + 7H^{+} = Fe^{+2} + 5Cu^{+} + 4H_2S + 0.25O_2
60	−13.1395	hematite + 4H^{+} = 2Fe^{+2} + 2 water + 0.5O_2
61	−11.9591	magnetite + 6H^{+} = 3Fe^{+2} + 3 water + 0.5O_2
		Log f_{O_2} vs. log $(a_{Fe^{+2}}/a^2_{Cu^{+}})$ (Fig. 5)
62	23.1844	2 chalcopyrite + 2H_2S + O_2 + Fe^{+2} = 3 pyrite + 2 water + 2Cu^{+}
63	15.9907	3 hematite + 4Cu^{+} + 8H_2S = 4 chalcopyrite + 2Fe^{+2} + 0.5O_2 + 8 water
64	−37.8719	4 bornite + 10Fe^{+2} + 16 water + 2.5O_2 = 7 hematite + 20Cu^{+} 16H_2S
65	2.98803	7 chalcocite + 2Fe^{+2} + H_2S + 0.5O_2 = 2 bornite + 4Cu^{+} + water
66	−49.6427	7 covellite + Fe^{+2} + 3 water = bornite + 1.5O_2 + 3H_2S + 2Cu^{+}
67	−26.9083	3.5 pyrite + 5Cu^{+} + 3 water = 2.5Fe^{+2} + 3H_2S + 1.5O_2 + bornite
68	−14.6105	2 covellite + water = chalcocite + H_2S + 0.5O_2
69	−111.059	6 bornite + 24 water + 2O_2 + 15Fe^{+2} = 7 magnetite + 30Cu^{+} + 24H_2S
70	−0.42027	3 bornite + 4Fe^{+2} + 2H_2S + O_2 = 7 chalcopyrite + 2 water + 8Cu^{+}
71	−38.9299	3 pyrite + 6 water = magnetite + 6H_2S + O_2
72	30.4227	3 pyrrhotite + 2Cu^{+} + H_2S + 0.5O_2 = Fe^{+2} + 2 chalcopyrite + water
73	−17.8690	pyrite + water = pyrrhotite + H_2S + 0.5O_2
74	−14.6772	magnetite + 3H_2S = 3 pyrrhotite + 3 water + 0.5O_2
75	−213.800	6 bornite + 3 water + 15Fe^{+2} = 21 pyrrhotite + 30Cu^{+} + 3H_2S + 1.5O_2
76	14.5850	magnetite + 6Cu^{+} + 3H_2S = 3 chalcocite + 3Fe^{+2} + 3 water + 0.5O_2
77	−33.7775	4 covellite + 2Fe^{+2} + 4 water = 4Cu^{+} + 4H_2S + hematite + 0.5O_2
78	−29.2622	3 chalcocite + 3Fe^{+2} = 3 pyrrhotite + 6Cu^{+}
79	−6.49553	2 covellite + Fe^{+2} = pyrite + 2Cu^{+}
80	−15.5004	3 hematite = 2 magnetite + 0.5O_2
81	20.7865	hematite + 4H_2S + 0.5O_2 = 4 water + 2 pyrite
82	−15.7455	2 chalcopyrite + 4 water + Fe^{+2} = magnetite + 2Cu^{+} + 4H_2S
		Annite stability field (Fig. 5)
83	32.2467	annite + 2Cu^{+} + 4H_2S + 0.5O_2 = orthoclase + 2 chalcopyrite + Fe^{+2} + 5 water
84	226.568	7 annite + 30Cu^{+} + 24H_2S + 1.5O_2 = 7 orthoclase + 6 bornite + 15Fe^{+2} + 31 water
85	31.0862	annite + 6Cu^{+} + 3H_2S = orthoclase + 3Fe^{+2} + 3 chalcocite + 4 water
86	1.82403	annite + 3H_2S = orthoclase + 3 pyrrhotite + 4 water
87	55.4311	annite + 6H_2S + 1.5O_2 = orthoclase + 3 pyrite + 7 water
13	16.5012	annite + 0.5O_2 = orthoclase + water + magnetite
		Sulfur-oxygen exchange reaction
88	12.1108	H_2S + 0.5O_2 = water + 0.5S_2
		Log f_{S_2} vs. log $(a_{Fe^{+2}}/a^2_{Cu^{+}})$ (Fig. 6)
89	−1.03718	2 chalcopyrite + Fe^{+2} + S_2 = 3 pyrite + 2Cu^{+}
90	28.1014	3 hematite + 4Cu^{+} + 9H_2S = 4 chalcopyrite + 2Fe^{+2} + 9 water + 0.5S_2
91	−98.426	4 bornite + 10Fe^{+2} + 21 water + 2.5S_2 = 7 hematite + 20Cu^{+} + 21H_2S
92	−9.1227	7 chalcocite + 2Fe^{+2} + 0.5S_2 = 2 bornite + 4Cu^{+}
93	−13.3104	7 covellite + Fe^{+2} = bornite + 2Cu^{+} + 1.5S_2
94	9.4240	3.5 pyrite + 5Cu^{+} = 2.5Fe^{+2} + bornite + 1.5S_2
6	−2.49972	2 covellite = chalcocite + 0.5S_2

TABLE 1.—(*Continued*)

Reaction no.	log K(t = 300°C, p = 500 bars)	
95	−159.502	6 bornite + 28 water + $2S_2$ + $15Fe^{+2}$ = 7 magnetite + $28H_2S$ + $30Cu^+$
96	−24.6418	3 bornite + $4Fe^{+2}$ + S_2 = 7 chalcopyrite + $8Cu^+$
97	−14.7083	3 pyrite + 4 water = magnetite + S_2 + $4H_2S$
98	18.3119	3 pyrrhotite + $2Cu^+$ + $0.5S_2$ = 2 chalcopyrite + Fe^{+2}
3	5.75826	pyrrhotite + $0.5S_2$ = pyrite
99	−2.56643	magnetite + $4H_2S$ = 3 pyrrhotite + 4 water + $0.5S_2$
100	−177.467	6 bornite + $15Fe^{+2}$ = 21 pyrrhotite + $30Cu^+$ + $1.5S_2$
101	−26.6958	3 chalcocite + 4 water + $3Fe^{+2}$ + $0.5S_2$ = magnetite + $4H_2S$ + $6Cu^+$
102	−21.6668	4 covellite + 3 water + $2Fe^{+2}$ = hematite + $4Cu^+$ + $0.5S_2$ + $3H_2S$
78	−29.2622	3 chalcocite + $3Fe^{+2}$ = 3 pyrrhotite + $6Cu^+$
79	−6.49553	2 covellite + Fe^{+2} = pyrite + $2Cu^+$
103	3.38959	2 magnetite + water + $0.5S_2$ = 3 hematite + H_2S
104	8.6757	hematite + $3H_2S$ + $0.5S_2$ = 3 water + 2 pyrite
82	−15.7455	2 chalcopyrite + 4 water + Fe^{+2} = magnetite + $2Cu^+$ + $4H_2S$
		Annite stability field
105	20.1360	annite + $2Cu^+$ + $3H_2S$ + $0.5S_2$ = orthoclase + 2 chalcopyrite + Fe^{+2} + 4 water
106	190.235	7 annite + $30Cu^+$ + $21H_2S$ + $1.5S_2$ = 7 orthoclase + 6 bornite + $15Fe^{+2}$ + 28 water
85	31.0862	annite + $6Cu^+$ + $3H_2S$ = orthoclase + $3Fe^{+2}$ + 3 chalcocite + 4 water
86	1.82403	annite + $3H_2S$ = orthoclase + 3 pyrrhotite + 4 water
107	19.0988	annite + $3H_2S$ + $1.5S_2$ = orthoclase + 3 pyrite + 4 water
108	4.39046	annite + $0.5S_2$ = orthoclase + magnetite + H_2S
		Alunite-kaolinite-muscovite-orthoclase diagram (Fig. 7)
15	−7.90771	muscovite + $2K^+$ + 6 quartz = 3 orthoclase + $2H^+$
16	7.58615	4 muscovite + $4H^+$ + 6 water = 6 kaolinite + $4K^+$
109	32.1024	3 kaolinite + $2K^+$ + $6H^+$ + $4SO_4^{-2}$ = 2 alunite + $6SiO_{2(aq)}$ + 3 water
110	17.9477	muscovite + $4H^+$ + $2SO_4^{-2}$ = alunite + $3SiO_{2(aq)}$
111	14.3699	3 orthoclase + $6H^+$ + $2SO_4^{-2}$ = alunite + $2K^+$ + $9SiO_{2(aq)}$
		Log f_{O_2} vs. log $(a_{Fe^{+2}}/a^2_{Cu^+})$ and log $f_{H_2S(g)}$ (Figs. 8–10)
		See reactions for Figure 5.

log f_{O_2}), magnetite (intermediate log $f_{O_2} - f_{S_2}$), and pyrrhotite at lowest log f_{O_2} and log f_{S_2}.

The stability field of biotite (annite-$KFe_3AlSi_3O_{10}(OH)_2$ component) is shown bounded by orthoclase. These equilibria are also given in Table 1 (reactions 11–13) and involve orthoclase-annite coexisting with pyrrhotite (lowest log f_{O_2} and f_{S_2}) (Putman, 1972, 1973; Tso et al., 1979), pyrite (highest log f_{S_2}), and magnetite (highest log f_{O_2}).

5 water

Depiction of protore assemblages

The protore mineral assemblages of the two porphyry copper models may now be depicted in a sulfur-oxygen fugacity diagram (Fig. 2). The deep peripheral chalcopyrite-pyrite-magnetite protore of the Lowell and Guilbert model with orthoclase and biotite is shown here by hexagon 1, which also represents the Butte pre-Main Stage protore assemblage (Brimhall, 1977, 1979). The deep central chalcopyrite-bornite ± magnetite protore with coexisting biotite and orthoclase is shown by hexagon 2. In contrast, both facies of protore in the diorite model cover broad areas in the fugacity diagram but, because of their general lack of orthoclase, are restricted to the annite field. The peripheral pyrrhotite-chalcopyrite assemblage is shown by hexagon 3, and the deep central bornite-magnetite assemblage by hexagon 4. In general, both dioritic protores seem to represent lower states of oxidation and sulfidation than their counterparts in monzonitic host rocks. Furthermore, within a given model, the peripheral bornite-deficient protores may represent higher sulfur fugacities than the deep core zones, or simply lower temperatures of formation.

Depiction of late-stage alteration assemblages

Products of hydrolitic attack of wall-rock protores are also shown in Figure 2. The simplest equilibrium involves muscovite-alunite (see Table 1, reaction 14). This phase boundary at the unit activity of water depends only upon log f_{S_2} and f_{O_2} values similar to the simple equilibrium already calculated. However, in order to represent musco-

ties of $H_2S_{(g)}$ with reaction details and equilibrium constants given in Table 1 (reactions 17–30). The strong dependence of many of the phase boundaries upon $\log f_{H_2S}$ is apparent in Figure 3, making it difficult to represent continuous reaction paths attending protore oxidation.

This problem has been overcome by using $\log f_{H_2S(g)}$ as an independent variable in the representation of phase equilibria in a new and useful fashion (Fig. 4), in which the ratio of the aqueous ferrous to cuprous ion activity-squared is used as a dependent variable independent of pH. Mineral triple points in Figure 3, e.g., magnetite-hematite-bornite (Fig. 3c), are expressed at a given $\log f_{H_2S(g)}$ by a $\log (a_{Fe^{+2}}/a^2_{Cu^+})$. Mineral hydrolysis reactions given in Table 1 (reactions 31–38) are used to compute the metal ion activity ratios corresponding to the triple points for three coexisting minerals. An example of such a calculation is useful. Consider the example at hand, i.e., Figure 3c, here the three pertinent hydrolysis reactions are magnetite, hematite, and bornite (Table 1, reactions 38, 37, and 36, respectively). As these reactions involve, in addition to H_2S, Cu^+, Fe^{+2}, and unwanted SO_4^{-2} and H^+ ions, the latter must be eliminated. This is done by balancing simultaneously on H^+ and SO_4^{-2}. Multiplying reactions 38, 37, and 36 by unknown stoichiometric reaction coefficients a, b, c, respectively, gives a solution for the H^+ balance ($5.5a + 3.5b + 6.75c = 0$) and the SO_4^{-2} balance ($0.25a + 0.25b + 0.125c = 0$) of $a = -2.5$ and $b = 2$, for $c = 1$. The equilibrium is then expressed as 1.0 bornite + 2 hematite + 2.5 Fe^{+2} + 4 H_2O = 2.5 magnetite + 5 Cu^+ + 4 $H_2S_{(g)}$. All such triple points in Figure 3 are recomputed and are given in Table 1 (reac-

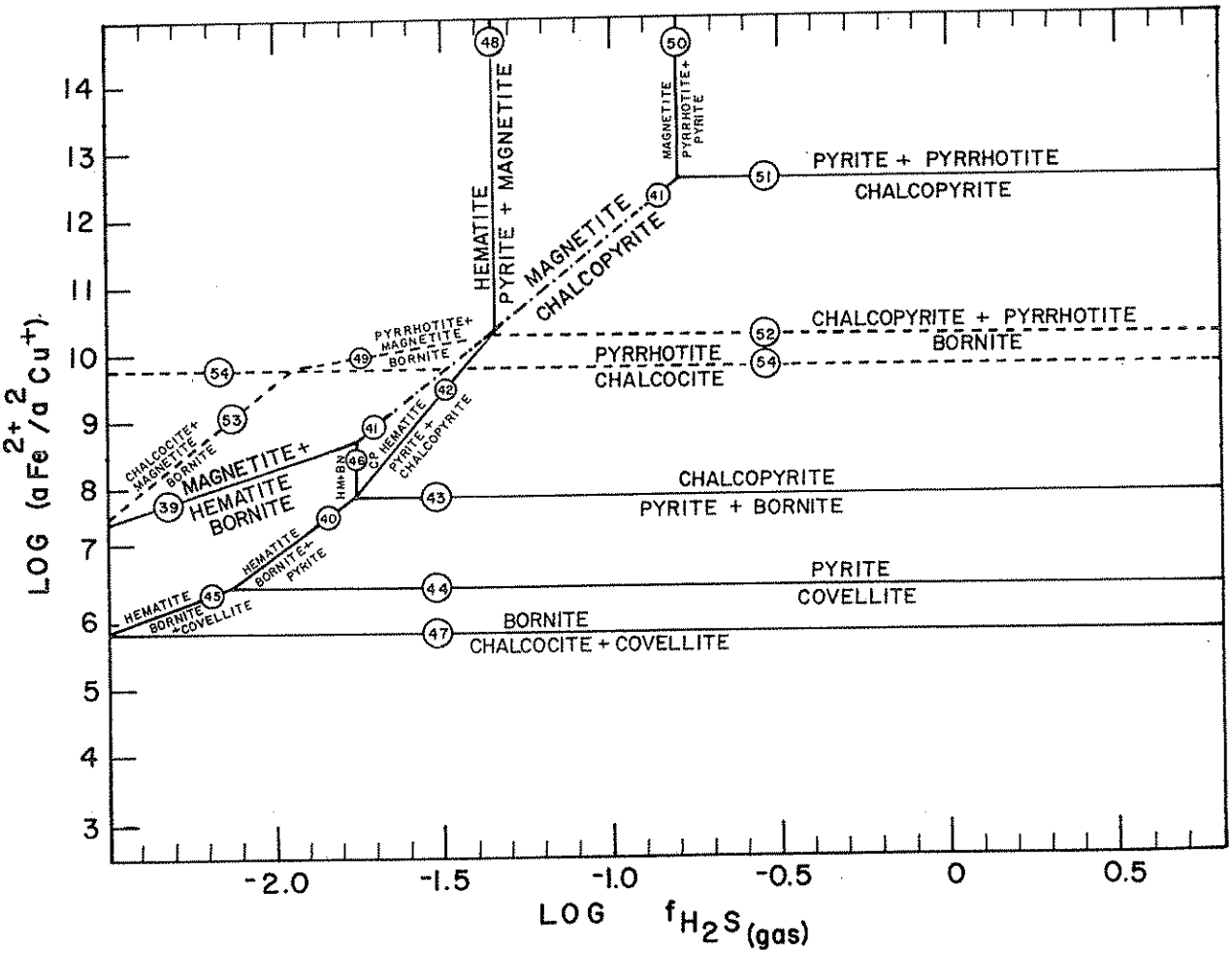

FIG. 4. Theoretical activity-fugacity diagram at 300°C and 500 bars representing the locus of triple points in Figure 3. Mineral hydrolysis reactions (31–38, Table 1) are balanced simultaneously on H^+ and SO_4^{-2} yielding mineral equilibria involving only $H_2S_{(g)}$ and $a_{Fe^{+2}}/a^2_{Cu^+}$. An example of the magnetite-hematite-bornite boundary (reaction 39 in Fig. 4) is included in the text to show the means of calculating reaction stoichiometry. Thermodynamic data are from Helgeson et al. (1974, 1978, 1980). Reactions and corresponding equilibrium constants are given in Table 1.

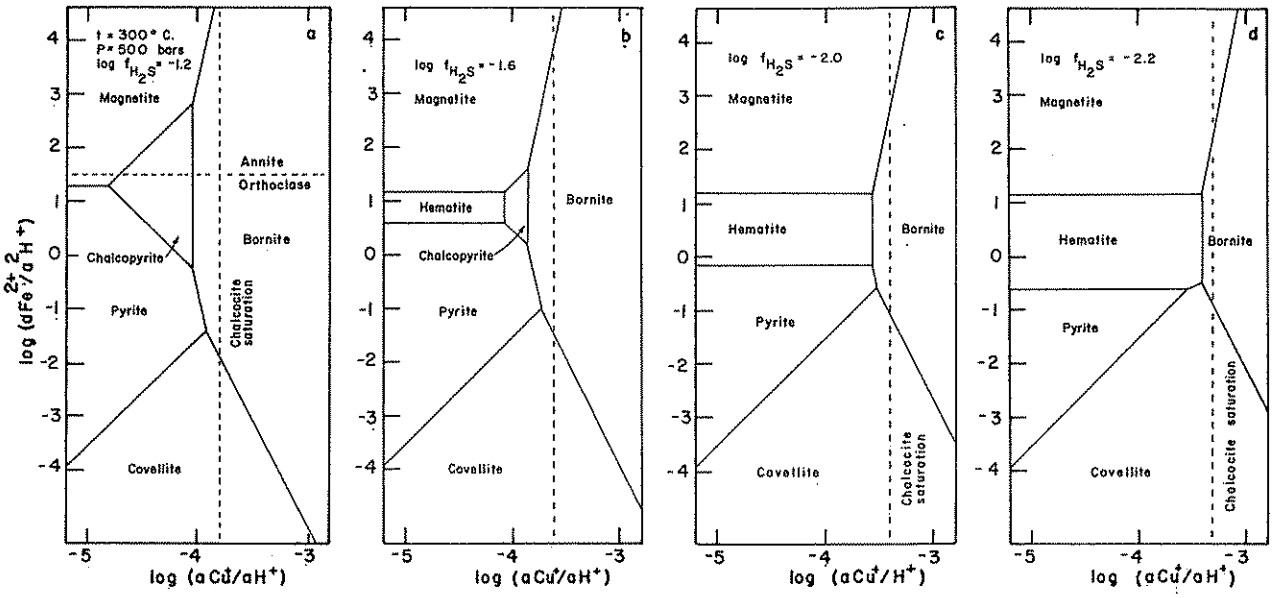

FIG. 3. Theoretical isothermal-isobaric activity diagrams at 300°C and 500 bars representing the stability fields of magnetite, chalcopyrite, pyrite, covellite, bornite, hematite, chalcocite, annite, and orthoclase at various $H_2S_{(g)}$ fugacities and unit activity $H_2O_{(liq)}$. Strong $H_2S_{(g)}$ fugacity dependence of many of the phase boundaries requires using this fugacity as an independent variable (see Fig. 4). Thermodynamic data of Helgeson et al. (1974, 1978, 1980) are used and reactions are given in Table 1.

vite-orthoclase or muscovite-kaolinite equilibria (Table 1, reactions 15 and 16) in Figure 2, it is necessary to graph the pH of the coexisting aqueous fluid in various parts of the diagram and to specify the total molality of KCl in the system by fixing $\log a_{K^+}$ (Montoya and Hemley, 1975). To this end, the dominant aqueous sulfur species have been shown in Figure 2 for a 0.01-molar total sulfur solution. The calculation methods of equal activity boundaries between dominant species has been discussed (Meyer and Hemley, 1967; Helgeson, 1969) and the thermodynamic data used are from Helgeson (1969), Helgeson et al. (1978), and Wolery (1979). There are, however, important differences between the dominant species shown here at 300°C and those given at 250°C in Meyer and Hemley (1967). There is at 300°C no intervening HS^- field between $H_2S_{(aq)}$ and S^{-2}. It is also evident in Figure 2 that $H_2S_{(aq)}$ is the dominant sulfur species in any fluid in equilibrium with chalcopyrite coexisting with other sulfides or oxides or in most domains of geological interest (Helgeson, 1969). Lines of constant pH have been constructed within the HSO_4^-, SO_4^{-2}, and S^{-2} fields which allow characterization of the orthoclase-muscovite and muscovite-kaolinite boundaries for a 1-molar total KCl solution (Montoya and Hemley, 1975; Einaudi, 1977).

Characterization of meteoric hydrothermal fluids

In their discussion of the chemical evolution of the Butte ore-forming fluid (Meyer et al., 1968; later treated in Sheppard and Taylor, 1974), the fluids causing advanced argillic alteration are thought to represent the original "pristine" late-stage, vein-forming fluid. As pointed out in the introduction, this fluid is fairly highly evolved but is probably very close to the composition of ore-forming fluids in veins. The composition of this highly oxidizing fluid is represented in Figure 2 by utilizing the common sulfide-silicate mineral assemblage of the advanced argillic assemblage occurring in the horsetail zones of the Butte district which are zones of extremely high fracture density and permeability. The advanced argillic assemblage is also found at the inner or veinward alteration zone adjoining many base metal veins. Covellite and chalcocite, often with pyrite, occur in muscovite-alunite assemblages, thus fixing the oxygen and sulfur fugacities of the oxidizing fluid as shown in Figure 2. It is then possible to determine from the phase diagram the differences in oxidation-sulfidation states between the oxidizing meteoric solution and the various protores of the porphyry copper environment.

Aqueous base metal activity diagrams

In addition to consideration of oxygen and sulfur gas-fugacity-dependent mineral equilibria, it is necessary, in order to understand base metal metasomatism, to depict phase stabilities in terms of aqueous base metal ion activities (Helgeson, 1970; Knight, 1977; Brimhall, 1979). Figure 3 shows important phase relations at various fugaci-

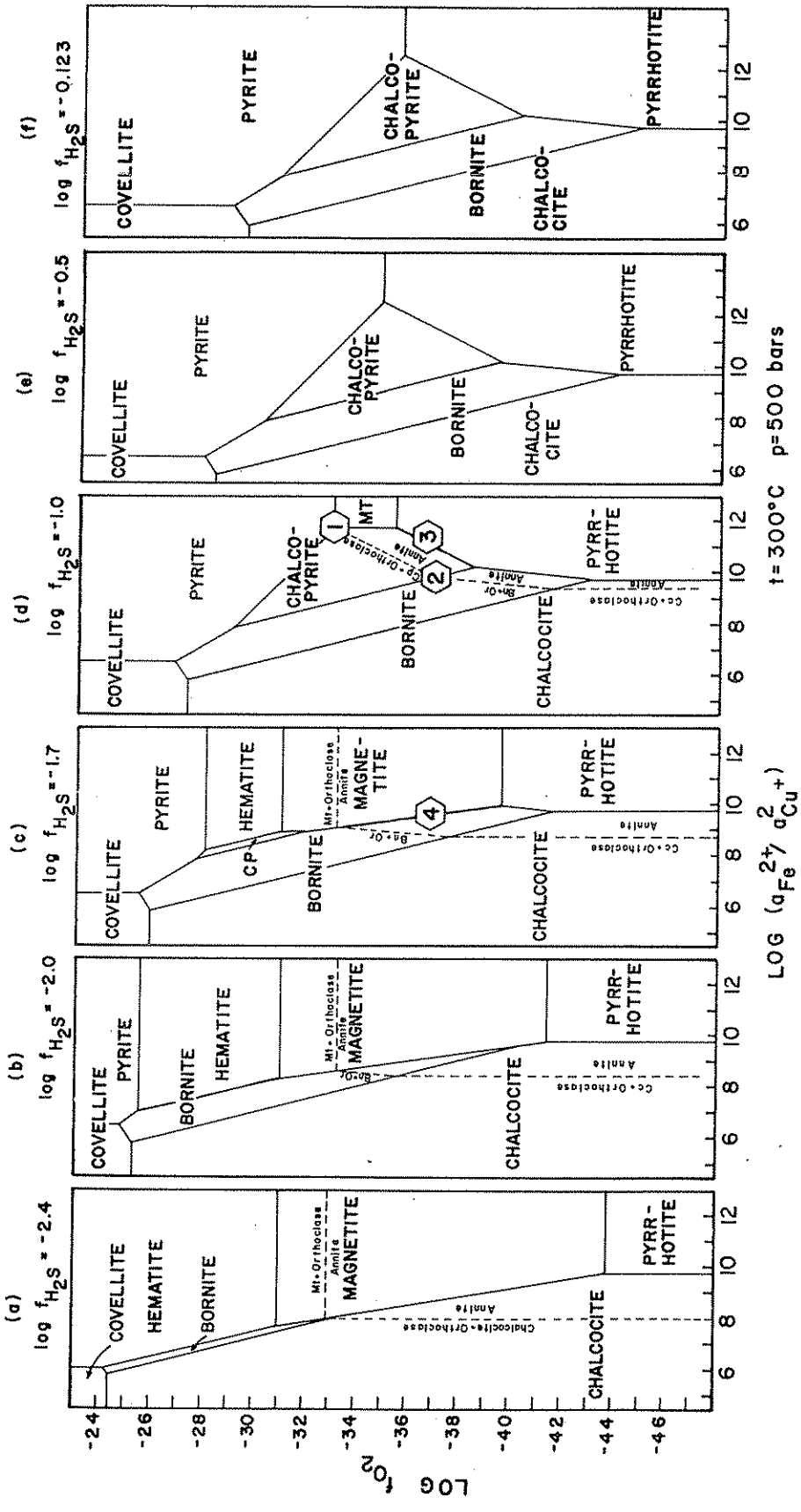

FIG. 5. Theoretical oxygen fugacity-activity diagrams at 300°C and 500 bars representing the sulfide and oxide stability fields for protores and oxidized reaction products. A through f are serial cross sections at the various $H_2S_{(g)}$ fugacities from Figure 4, with $\log f_{O_2}$ as the vertical axis. Protores 1 and 2 of the Lowell and Guilbert (1970) and 3 and 4 of the diorite model (Hollister, 1978) are shown as hexagons (see Fig. 2 for mineralogic details). Notice that covellite and pyrite are present only at the highest oxygen fugacities. The phase boundary between pyrite and covellite depends only on $\log (a_{Fe^{+2}}/a^2_{Cu^+})$ and not on $\log f_{H_2S(g)}$ (see Fig. 4). Thermodynamic data are from Helgeson et al. (1974, 1978, 1980). Table 1 presents reaction stoichiometry and corresponding equilibrium constants. Notice the parallelism of the annite-orthoclase phase boundary and the pyrrhotite field.

tions 39–54), including the pyrrhotite-bearing assemblages.

It is now possible by examining Figure 4 to visualize the iron to copper ion activity ratios for various sulfide and oxide assemblages over a wide and continuous range of $H_2S_{(g)}$ fugacities. Because $H_2S_{(aq)}$, related to $H_2S_{(g)}$ as shown in Figure 4, is the dominant aqueous sulfur species at these conditions, the abscissa has an important geological significance. We see, for example, over the full range of $\log f_{H_2S(g)}$ that chalcocite-covellite assemblages occur at very low iron to copper activity ratios. In contrast, magnetite-hematite-bearing assemblages occur only at relatively low $\log f_{H_2S(g)}$ values and at high iron to copper activity ratios.

It is useful to interpret the equilibria expressed in Figure 4 in terms of oxygen and sulfur fugacities. This is readily accomplished by combining an oxygen-sulfate ion exchange reaction (Table 1, reaction 55) with each hydrolysis reaction (Table 1, reactions 31–38) eliminating H^+ and SO_4^{-2} from the reactions. The resultant oxidation reactions (Table 1, reactions 56–61) are then used to calculate phase boundaries between mineral pairs (Table 1, reactions 62–82).

These oxidation equilibria expressed as functions of iron to copper ion activity ratios for a given $\log f_{H_2S(g)}$ are presented in Figure 5. Each diagram in Figure 5 is a cross section through Figure 4 for specific $\log f_{H_2S(g)}$ values, i.e., -2.4, -2.0, -1.7, -1.0, -0.5, and -0.123. Each triple point in Figure 5a through f is represented in Figure 4 by a line or more precisely a linear function of $\log (a_{Fe^{+2}}/a^2_{Cu^+}) - \log f_{H_2S(g)}$.

Oxygen fugacity mineral buffers as well as buffer assemblages for $\log (a_{Fe^{+2}}/a^2_{Cu^+})$ are seen in Figure 5. The magnetite-hematite phase boundary is shown at a constant $\log f_{O_2}$ of approximately -31 occurring only at $\log f_{H_2S(g)}$ values less than -1.35. Above this $H_2S_{(g)}$ fugacity, hematite is not stable (see Fig. 4). Buffer assemblages for $\log (a_{Fe^{+2}}/a^2_{Cu^+})$ are covellite-pyrite and chalcocite-pyrrhotite at extremely high and extremely low oxygen fugacities, respectively, covering a wide range of H_2S fugacities. The remaining phase boundaries in Figure 5 are not strict buffer assemblages for either $\log f_{O_2}$ or $\log (a_{Fe^{+2}}/a^2_{Cu^+})$.

An interesting and significant parallelism occurs between $\log f_{O_2} - \log (a_{Fe^{+2}}/a^2_{Cu^+})$ relationships for sulfide and combined sulfide-silicate assemblages (e.g., Fig. 5d; Table 1, reactions 83–87). The stability field of annite is represented in Figure 5a through d. The phase boundary of bornite-orthoclase-annite parallels that of bornite-pyrrhotite, and the phase boundary of chalcopyrite-orthoclase-annite parallels that of chalcopyrite-pyrrhotite. It is significant that the phase boundary of annite with orthoclase plus additional sulfides and oxides parallels, but is displaced from, the pyrrhotite field. In other words, pyrrhotite is stable at 300°C with annite and not with orthoclase regardless of the H_2S fugacity. Although rare in the Lowell and Guilbert system, this incompatibility of orthoclase and pyrrhotite is consistent with the paucity of orthoclase and the dominance of biotite in the diorite model of porphyry copper systems, in which pyrrhotite is often an important phase. Diorite model protores are shown in Figure 5 at points 3 (chalcopyrite-pyrrhotite) and 4 (bornite-magnetite). For comparison, the Lowell and Guilbert model protores with coexisting annite-orthoclase are shown at 1 (pyrite-chalcopyrite) and 2 (chalcopyrite-bornite).

The sulfidation states, in addition to those involving oxidation, are useful in characterizing the mineral equilibria in the protores and oxidizing fluids as shown in Figure 2. Reactions 62 through 87, involving $\log f_{O_2}$, may be easily converted to reactions involving $\log f_{S_2}$ by combination with an oxygen-sulfur exchange reaction (Table 1, 88), $H_2S + \frac{1}{2}O_2 = H_2O + \frac{1}{2}S_2$. The resultant equilibria (Table 1, reactions 89–108) are shown graphically in Figure 6. It is important to recognize the identical topologies in Figures 5 and 6. The triple points occur at the same values of $\log (a_{Fe^{+2}}/a^2_{Cu^+})$ in both diagrams, but the $\log f_{O_2}$ and $\log f_{S_2}$ values are different because of reaction 88. Both Figures 5 and 6 are identical cross sections in Figure 4 at different $\log f_{H_2S}$ values. Notice in Figure 6d that the parallelism of the silicate-sulfide equilibria with the sulfide assemblages can still be seen, showing that the annite stability field is a closed volume with the Lowell and Guilbert protores occurring at its surface and the diorite model protores occurring within its interior, free of orthoclase. It is important also to recognize that pyrite is the mineral formed at the highest f_{O_2} and f_{S_2}. Chalcopyrite and bornite are both unstable at extremely high oxidation and sulfidation states.

Composition of the Oxidizing Advanced Argillic Fluid

As previously mentioned, the advanced argillic assemblage is characterized by the assemblage muscovite-alunite-kaolinite-quartz, often with chalcocite and covellite as in the Butte district. In addition to determining the sulfur and oxygen fugacities attending this assemblage (Fig. 2), it is possible to determine many other important solution composition parameters of geological importance during oxidation. Hemley et al. (1969)

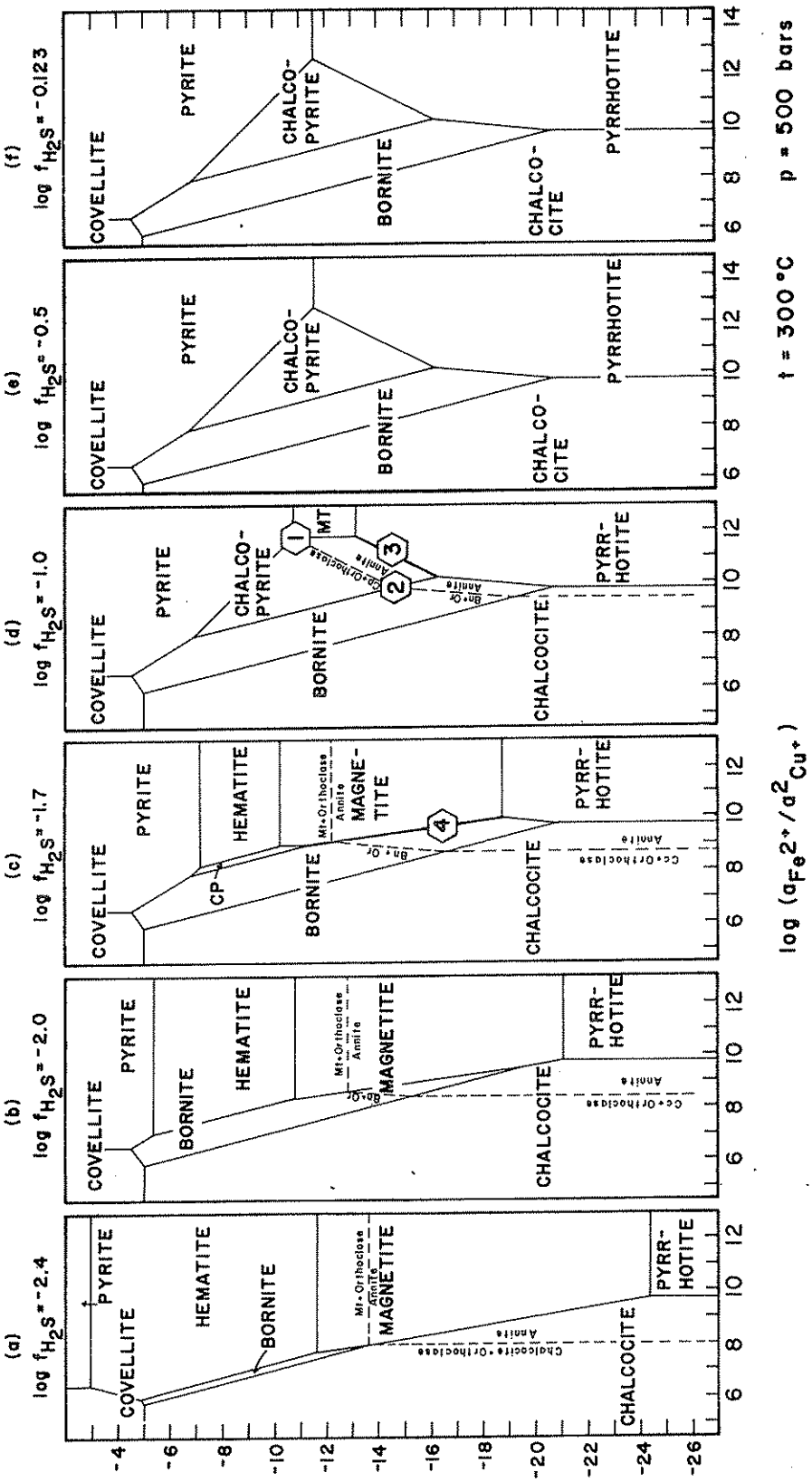

FIG. 6. Theoretical sulfur fugacity activity diagram at 300°C and 500 bars representing sulfide and oxide stability fields for protores and sulfidized reaction products. A through f are serial cross sections at the various $H_2S_{(g)}$ fugacities from Figure 4 with log $f_{S_{2(g)}}$ as the vertical axis. Protores 1 and 2 of the Lowell and Guilbert (1970) and 3 and 4 of the diorite model (Hollister, 1978) are shown as hexagons (see Fig. 2 for mineralogic details). Notice that covellite and pyrite are present at highest sulfur fugacities. Notice also the parallelism of the annite-orthoclase phase boundary and the pyrrhotite field. Thermodynamic data are from Helgeson et al. (1974, 1978, 1980). Table 1 presents the reaction stoichiometry and corresponding equilibrium constants.

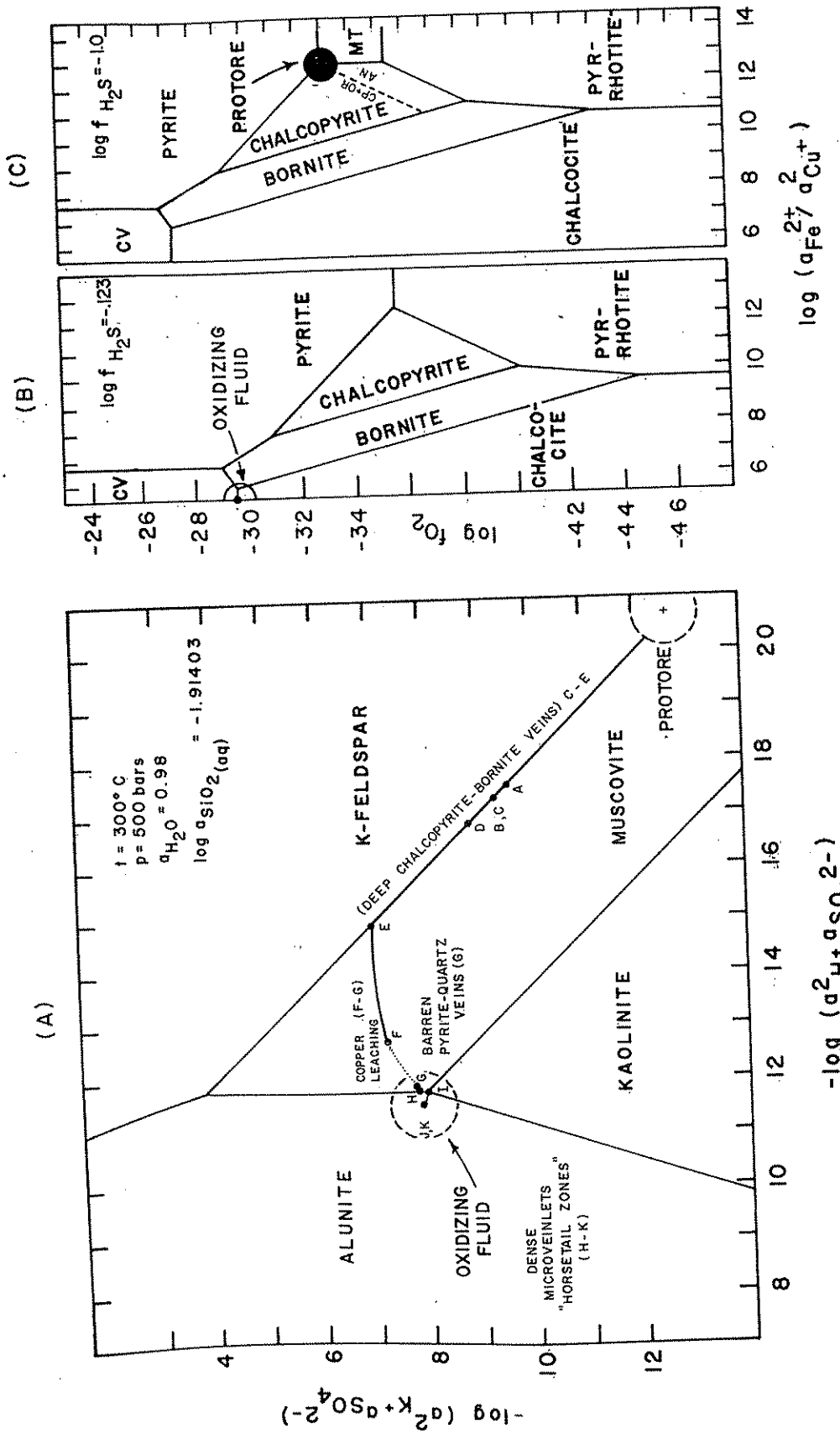

FIG. 7. Graphical representation of the composition of the oxidizing advanced argillic fluid (Fig. 7A and B) and wall-rock protore assemblage (Fig. 7A and C) constructed at 300°C and 500 bars; thermodynamic data are from Helgeson et al. (1974, 1978, 1980). The advanced assemblage described by Hemley et al. (1969) is shown as the triple point alunite, kaolinite, and muscovite. Computed reaction path A–K is shown for a chalcopyrite-pyrite-magnetite (the Lowell and Guilbert model) K-silicate protore (see Fig. 13). Intense copper leaching and barren pyrite-quartz veins are shown from F–G.

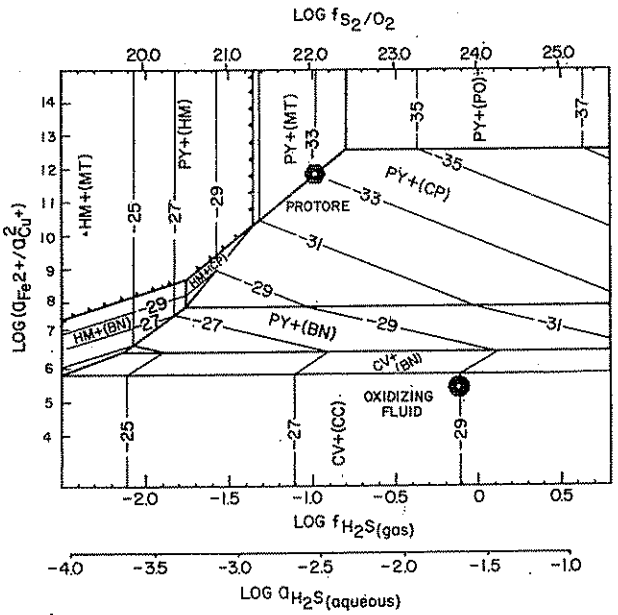

FIG. 8. Base metal activity ratio-$H_2S_{(g)}$ fugacity diagram contoured on $\log f_{O_{2(g)}}$ for uppermost phase boundaries (surfaces) in Figure 5, constructed at 300°C and 500 bars. A topographic surface with $\log f_{O_2}$ as the vertical axis is represented. The superadjacent mineral is shown for each surface and the subjacent mineral is shown in parentheses. The composition of the oxidizing advanced argillic solution is shown as a solid circle positioned on the covellite-chalcocite phase boundary with a $\log f_{O_2}$ near −29. Covellite occurs above this surface and chalcocite below. The chalcopyrite-pyrite-magnetite protore is shown as a solid hexagon at a $\log f_{O_2}$ near −33. The $\log f_{H_2S_{(g)}}$ is related directly to $\log f_{S_2}/f_{O_2}$ and to $\log f_{H_2S_{(aq)}}$. See Table 1 for details. The magnetite-hematite f_{O_2} buffer is a horizontal plane bounded by solid triangles at a $\log f_{O_2}$ of about −31.

determined that at quartz saturation and 300°C at 15,000 bars, the assemblage alunite-muscovite-kaolinite fixed the solution pH at a value of 3.17. Using the data of Helgeson et al. (1978), Figure 7A (Table 1, reactions 109–111 and 15–16) has been constructed showing the stability fields of important alteration minerals at the highly oxidizing and sulfidizing conditions of the advanced argillic assemblage depicted in Figure 2 at a $\log f_{S_2}$ of approximately −5.0 and a $\log f_{O_2} = 29.0$. Aqueous ion activities are then calculated for the triple point, alunite-muscovite-kaolinite, giving $\log a_{SO_4^{-2}} = -5.29$ and $\log a_{K^+} = -1.26$. Using reaction 55, $H_2S_{(g)} + 2O_2 = 2H^+ + SO_4^{-2}$, and already knowing the oxygen fugacity, pH, and sulfate activity, it is possible to determine $\log f_{H_2S_{(g)}}$ as −0.123. Bisulfide ion activity may be calculated from the H_2S dissociation as $\log a_{HS^-} = -6.33$. Cuprous ion activity is determined at chalcocite saturation (reaction 34): chalcocite + $2H^+ = 2Cu^+ + H_2S_{(g)}$ yielding $\log a_{Cu^+} = -7.48$. Figure 4 is used to determine the ferrous ion activity. It is seen in Figure 4 that chalcocite and covellite coexist only at $\log (a_{Fe^{+2}}/a^2_{Cu^+})$ values less than 6.3, thus limiting the range of possibilities for $\log a_{Fe^{+2}}$. A ratio of 5.5, corresponding to $\log a_{Fe^{+2}} = -9.46$, has been chosen for this study. Figure 7B and C depict the composition of the oxidizing aqueous fluid and the chalcopyrite-pyrite-magnetite orthoclase-annite protore. It is obvious that there is a difference between these two states in oxygen fugacity of three orders of magnitude, and seven orders of magnitude in $\log (a_{Fe^{+2}}/a^2_{Cu^+})$. In order to illustrate graphically the reaction paths attending a strong oxidation of protores, it is therefore necessary to depict both of these parameters, as well as the H_2S fugacity, since $H_2S_{(aq)}$ is the dominant sulfur species in solution.

Realizing that Figure 5 depicts a series of cross sections in Figure 4, it is a simple matter to generate a three-dimensional phase diagram with $\log f_{H_2S_{(g)}}$, $\log (a_{Fe^{+2}}/a^2_{Cu^+})$, and $\log f_{O_2}$ as the X, Y, and Z coordinates, respectively. Figure 8 shows such a diagram in which entire reaction paths of oxidation are depicted. It is clear in Figure 5 that multiple f_{O_2} surfaces exist for the same value of $\log a_{Fe^{+2}}/a^2_{Cu^+}$. This problem is overcome by constructing $\log f_{O_2}$ surfaces in two different diagrams, Figures 8 and 9, the former at high oxygen fugacities and the latter at low oxygen fugacities. In both diagrams (Figs. 8 and 9), each f_{O_2} surface is represented by two minerals, one above the plane of phase boundary and one below, indicated in parentheses. Reactions

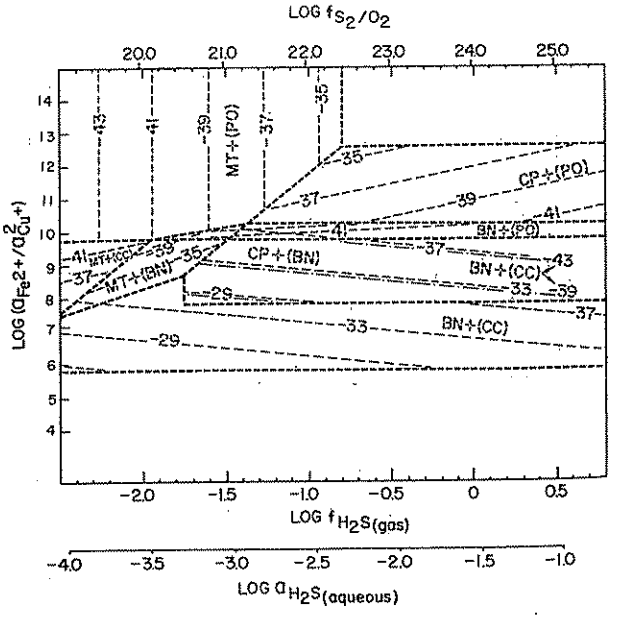

FIG. 9. Base metal activity ratio-$H_2S_{(g)}$ fugacity diagram contoured on $\log f_{O_{2(g)}}$ for the lower f_{O_2} phase boundaries in Figure 5. Figures 8 and 9 may be superimposed to obtain a full three-dimensional representation of the equilibria in the Cu-Fe-S-O-H system at 300°C and 500 bars.

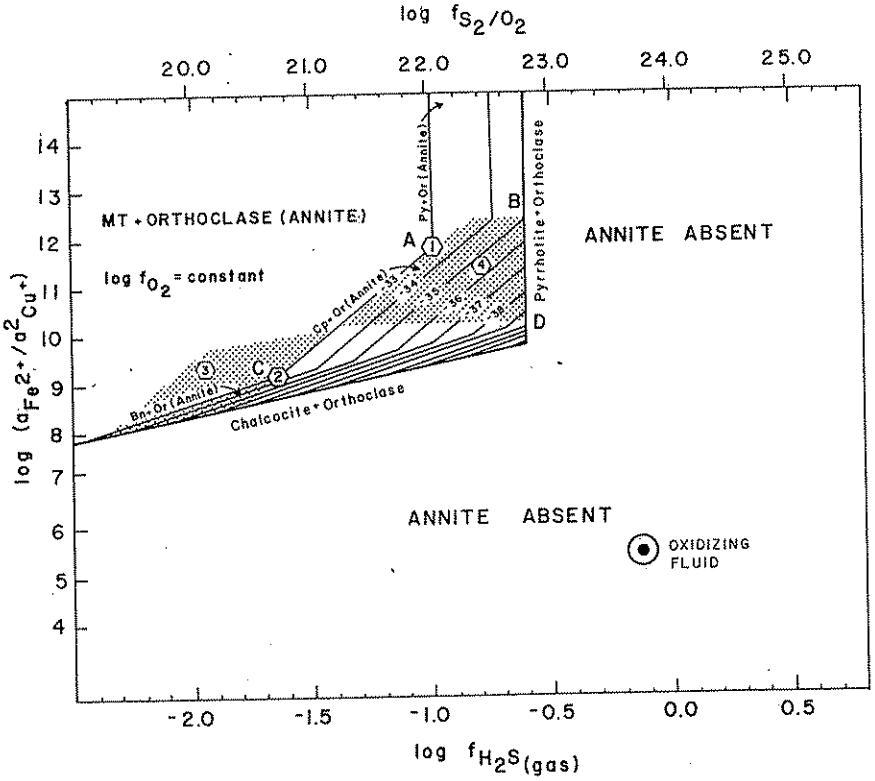

FIG. 10. Base metal activity-$H_2S_{(g)}$ fugacity diagram constructed at 300°C and 500 bars contoured on log f_{O_2} for the annite stability field, which occurs as a volume within this figure. The volume has a flat top bounded by the orthoclase + magnetite (annite) oxygen fugacity buffer. Minerals subjacent to each surface are shown in parentheses, e.g., annite. The annite phase volume has faceted sides represented by the assemblages bornite+orthoclase (annite), chalcocite+orthoclase (annite), pyrrhotite + orthoclase (annite), chalcopyrite + orthoclase (annite), and pyrite + orthoclase (annite). Annite is not stable at $\log f_{H_2S(g)}$ values greater than −0.6 nor at low $\log (a_{Fe^{+2}}/a^2_{Cu^+})$ activities. Protore assemblages for the Lowell and Guilbert (1970) model containing both annite and orthoclase are shown directly on the annite field surface at points 1 (chalcopyrite-pyrite-magnetite) and 2 (bornite-chalcopyrite-magnetite). Assemblages corresponding to these protores but differing only in a lack of magnetite occur along lines A-B and C-D, respectively. Protore assemblages for the diorite model (Hollister, 1978) are shown within the annite field since they lack orthoclase. The chalcopyrite-pyrrhotite (3) and bornite-magnetite (4) protores are depicted using a dotted pattern (see Fig. 9). The composition of the oxidizing advanced argillic fluids with a $\log f_{O_2}$ of −29 is shown. Thermodynamic data are from Helgeson et al. (1978). See Table 1 for the reaction stoichiometry and equilibrium constants used.

used to construct the log f_{O_2} contours are the same as for Figure 5 (Table 1, reactions 62–82). As the diagrams are geometrically quite involved, certain details should be explained. The magnetite-hematite oxygen fugacity buffer appears in Figure 8 as a horizontal plane limited in plan by the equilibria in Figure 4. These boundaries are shown in Figure 8 as heavy solid lines with solid triangles. The abscissa in Figure 8 is $\log f_{H_2S(g)}$ which is easily converted to $\log a_{H_2S(aq)}$ through the reaction $H_2S_{(g)} = H_2S_{(aq)}$, with a log at $K_{300°C} = -1.55$.

The composition of the oxidizing fluid is shown in Figure 8 as a circle. The pyrite-chalcopyrite-magnetite protore, in contrast, is shown as a hexagon. This point has been determined by solving simultaneously the equilibrium constant expressions of reactions 41 and 87, stipulating coexisting magnetite-chalcopyrite-annite-orthoclase. The oxygen fugacity derived is $\log f_{O_2} = -33.00$. The $\log (a_{Fe^{+2}}/a^2_{Cu^+})$ and $\log f_{H_2S(g)}$ coordinates of this protore are found by solving equilibrium constant expressions for reactions 62 and 41 giving $\log (a_{Fe^{+2}}/a^2_{Cu^+}) = 11.8$ and $\log f_{H_2S(g)} = -0.99$.

The extreme fluid compositions are shown in Figure 8, i.e., the unaltered fresh K-silicate chalcopyrite-pyrite-magnetite protore (hexagon) and the oxidizing fluid (circle). Chemical reaction between these two compositions involves oxidation, sulfidation, silicate hydrolysis, and base metal interchange between the aqueous phase and the mineral phases present at any given state of the reaction. The exact reaction path taken is essentially prescribed by the composition of the protore and oxidizing fluid. Different protores plot at different positions

in Figure 8 and will obviously have distinct reaction paths.

Annite Stability Field

The stability field of annite is centrally important in describing the various protores of the porphyry copper environment. In addition, the biotitic assemblages may buffer fluid compositions of circulating meteoric water until the protore buffer assemblage is destroyed. Thus it is necessary to understand the geometrical relationship of the annite field to other phase boundaries in the system Cu-Fe-O-H. Figure 10 has been constructed to give a three-dimensional representation of the annite stability field by combining Figures 5 and 8. Contours of $\log f_{O_2}$ are shown for coexisting annite-orthoclase with the sulfides and oxides stable in different $\log (a_{Fe^{++}}/a^2_{Cu^+}) - \log f_{H_2S}$ regions of the diagram. The annite field may be envisaged as a flat-topped, nearly rectangular volume with beveled edges. The four protore assemblages are depicted in relation to the annite field. The diorite model protores (3 and 4) are shown within the annite volume as dotted fields and the Lowell and Guilbert model protores are on the annite-orthoclase surface itself (1 and 2). In the latter model, magnetite-bearing protores are shown at points A and C for the chalcopyrite-pyrite and chalcopyrite-bornite protores. Assemblages lacking magnetite occur along the lines A-B and C-D for these same two protores. It is obviously worth noting with respect to natural biotites, which have in addition to ferrous iron, ferric iron plus magnesium, that the corresponding protore oxygen fugacity is different from that for pure annite. However, any protore with magnetite has a very restricted range of oxygen fugacities, i.e., below the hematite-magnetite buffer which fixes f_{O_2} below 10^{-31} (Figs. 8 and 2) regardless of the biotite composition.

Theoretical Evaluation of Reaction Paths

Thermodynamic and kinetic principles presently exist which are necessary to predict irreversible reactions in the present context within idealized closed chemical systems (Helgeson, 1968, 1971; Helgeson et al., 1969). A matrix algebraic method is used to describe mass transfer in geochemical processes by solving differential equations providing for simultaneous dissolution of multiple reactant minerals as well as mineral precipitation. Computer calculations involving a specified reactant mineral assemblage and solution composition are used to predict the extent to which minerals are produced or destroyed, in addition to changes in composition of the solid and aqueous phases (Helgeson et al., 1970). Computer programs used in the present study are from Wolery (1979) and include a program for the speciation of the aqueous phase, EQ3, and a path prediction program, EQ6. Possible errors in thermodynamic data used in these calculations may be greater for aqueous species than for the minerals considered. Zinc minerals and aqueous species have not been incorporated into the present study.

Four types of protore assemblages have been used in theoretical computations of oxidation by advanced argillic fluids at 300°C and 500 bars.

Butte protore

The first assemblage corresponds to one of the chalcopyrite-pyrite-magnetite protores analyzed from Butte drilling assay pulps discussed in Brimhall (1979, p. 571, 573, and 574). The molar abundances and relative reaction rates have been determined lithologically (Brimhall, 1979) and are used directly in the computer calculations of this study: chalcopyrite (1.0), biotite (0.95), hematite (0.20), magnetite (0.15), orthoclase (10.0), kaolinite (12.26), pyrite (5.0), and quartz (60.0). Incipient argillic alteration was found to have converted plagioclase in this protore to kaolinite before modification of any of the remaining minerals occurred. Theoretical reaction paths therefore apply in this instance to events following argillization of K-silicate protore. The relative reaction rates used are equal to the negative of the molar abundance, except for quartz and pyrite which had rates of 0.0 because they occur later as product minerals. The computed results of theoretically reacting oxidizing advanced argillic solutions with incipiently altered Butte protore are shown in Figure 11. The abscissa is a log mass ratio (fluid/reacted rock) which is of greater physical significance to most geologists than the reaction progress variable (ξ). Actual calculations were performed from right to left in the diagram for 1.0 kg of fluid. Presented in Figure 11 as functions of the fluid/rock ratio are modal mineral variations, copper content of idealized rock and fluid, fugacities of oxygen and sulfur in the fluid, and solution pH. Points of special interest are shown by letters A through L and are also indicated in Figure 12A.

The modal variation diagram shows the progressive destruction of the protore mineral assemblage at a fluid/rock ratio of 1.0 (point D) as muscovitization occurs with magnetite oxidation to hematite. Pyrite forms between fluid/rock ratios of 1 to 2.5 (B-H) and overlaps bornite formation from F to H in a fashion very similar to the sequence found geologically (Brimhall, 1979, p. 571 and 573).

Chalcocite and covellite formation occurs only at very high fluid/rock ratios following alunite deposition in the advanced argillic alteration assemblage including pyrophyllite.

Accompanying the modal mineralogic changes from protore to advanced argillic assemblage are important chemical variations. The copper content of the rock decreases from point B to a minimum of zero at D. This leaching behavior, caused by progressive chalcopyrite dissolution, confirms the lithological conclusions made earlier in Brimhall (1979). Notice also that the copper content of the fluid reaches a maximum value over this leaching interval and diminishes at higher fluid/rock ratios as bornite, chalcocite, and covellite form. Progressive oxidation and sulfidation are shown as stair-step functions in $\log f_{O_2}$ and $\log f_{S_2}$. Mineral buffer assemblages result in constant fugacities over distinct intervals of fluid/rock ratio but, because one or more of the minerals are destroyed as seen in modal variation, fugacities are free to change. Sulfur fugacity increases from low values in the protore to a value six order of magnitude higher in the advanced argillic assemblage (H). Oxygen fugacity increases initially, attains a value determined by the magnetite-hematite buffer (at A), and continues to increase as magnetite is destroyed. Between D and E a maximum in oxygen fugacity is reached where hematite dissolves liberating abundant oxygen into the solution as pyrite forms accompanied only by muscovite and quartz. It is significant that this state of highest oxygen fugacity, or peroxidation, corresponds to the interval in the fluid/rock ratio during which all copper is leached from the rock. This geologically significant reaction interval characterized by the barren quartz-pyrite-(hematite) assemblage is shown in Figure 12A by plus signs which indicate oxygen fugacities in the pyrite field above the pyrite-chalcopyrite or pyrite-bornite phase boundaries.

Quartz monzonite protore

Chemical interaction of a plagioclase-bearing chalcopyrite-pyrite-magnetite protore in a quartz monzonite wall rock with the oxidizing advanced argillic fluid has been computed. The results are presented in Figure 13 and in many respects differ little from those depicted in Figure 11, except that, in the former, plagioclase is a reactant instead of kaolinite. The modal data for the quartz monzonite are shown in Table 2, column A. The corresponding modal abundances are chalcopyrite (1.0), annite (for biotite, 3.49), magnetite (1.97),

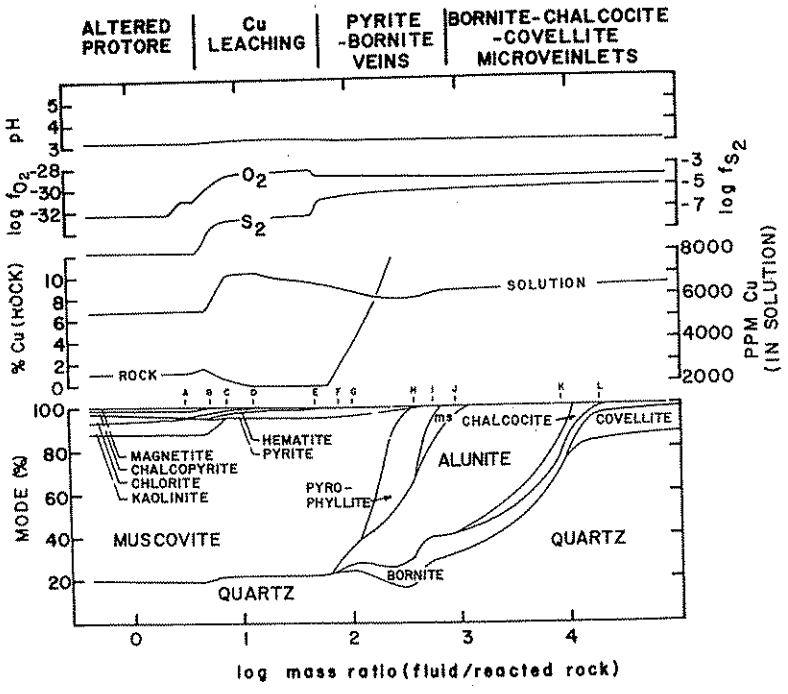

FIG. 11. Calculated mineralogical and chemical effects of interacting oxidizing advanced argillic fluids with clay-altered chalcopyrite-pyrite-magnetite protore at 300°C and 500 bars. Relative reaction rates used in the calculations come from a lithologic study of the Butte district, Montana (Brimhall, 1979). Computer programs used in the path calculations are from Wolery (1979) using the thermodynamic data of Helgeson et al. (1978). The abscissa is relative to 1,000 g of fluid. Sequence letters A–L depict the reaction path shown in Figure 12A.

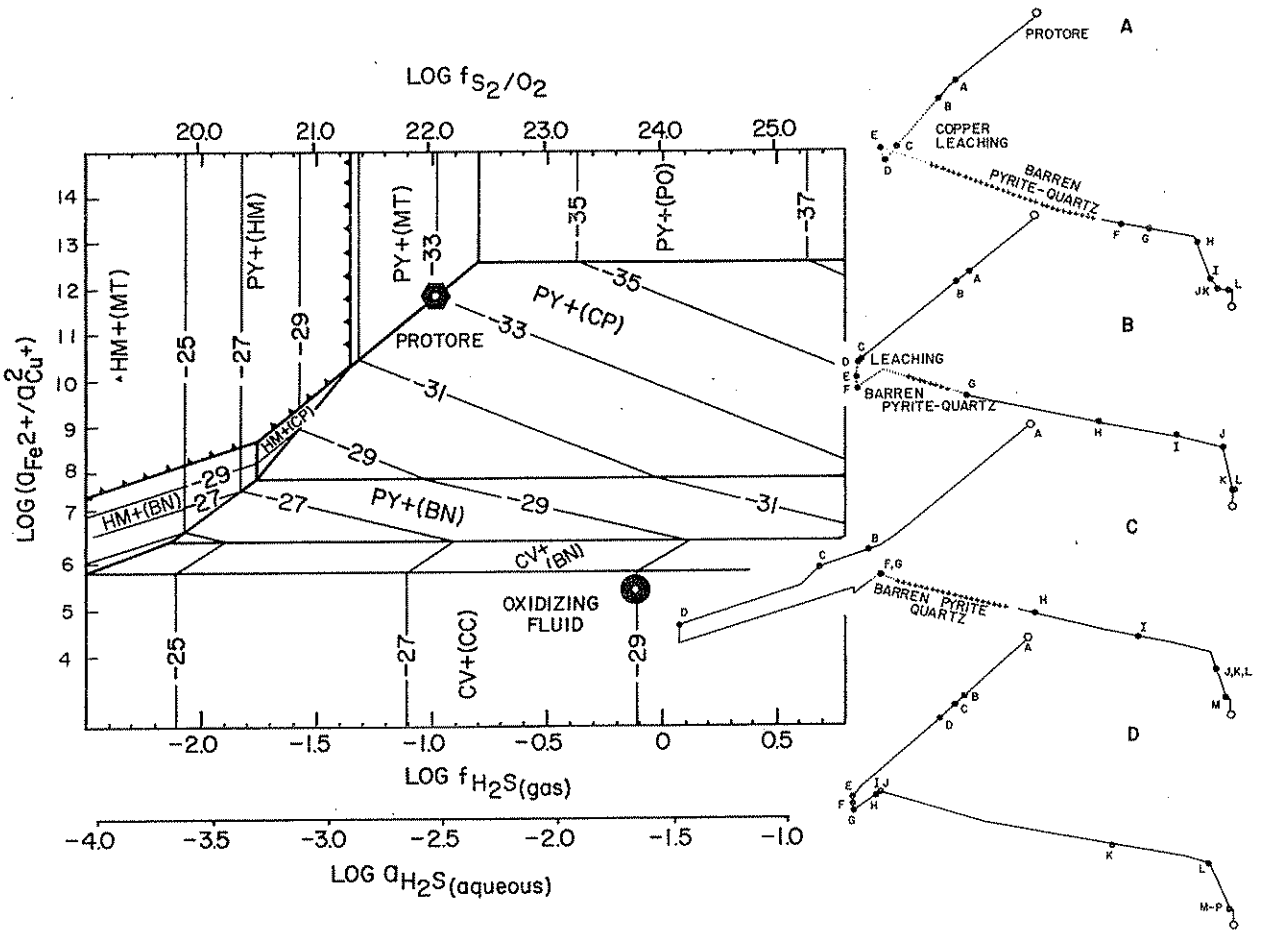

FIG. 12. Calculated reaction paths derived by reacting oxidizing advanced argillic fluids (circle) and various protores: A, a chalcopyrite-pyrite-magnetite protore with clay-altered plagioclase (Brimhall, 1979); B, a fresh K-silicate protore containing chalcopyrite-pyrite-magnetite (point 1 in Figs. 2, 5, 7, 8, and 10); C, a diorite containing a chalcopyrite-pyrrhotite assemblage (point 3 in Figs. 2, 5, 7, 8, and 10); and D, a chalcopyrite-pyrite protore, similar to B but lacking magnetite. Copper leaching is represented by a dotted pattern; barren pyrite-quartz assemblages are shown by plus signs, and indicate peroxidizing O_2 fugacities in the pyrite field above the py (cp) or py (bn) phase boundaries. Reaction paths may be copied onto a piece of tracing paper and positioned on the main part of the figure, using the composition of the oxidizing fluid for reference. Abbreviations: AN, annite; BN, bornite; CP, chalcopyrite; CV, covellite; HM, hematite; MT, magnetite; OR, orthoclase; PO, pyrrhotite; PY, pyrite.

orthoclase (8.89), pyrite (5.48), quartz (44.45), and low albite (for plagioclase, 16.22). The relative reaction rates used are equal to the negative of the molar abundances. Although intermediate plagioclase, e.g., andesine, is the common feldspar in monzonites, no activity coefficient data are presently available for low temperatures, thus necessitating the use of albite in the computations.

Points of special interest in Figure 13 have been denoted by the letters A through K, shown also in Figures 2, 7A, and 12B for the monzonite model. As the computed fluid/rock ratio increases, the computed reaction path is then easily seen in each of these figures. The oxidation steps occurring as the protore f_{O_2} buffers are progressively destroyed (Fig. 13) can be understood by following the reaction path in Figure 12B. The first interval of the reaction, between the protore and point A, involves the destruction of annite. The solution composition is driven to A along the magnetite-chalcopyrite-pyrite phase boundary from $\log f_{O_2} = -33$ to -31. At B hematite starts to form fixing the oxygen fugacity at 10^{-31} where it remains until point C is reached where all magnetite is oxidized to hematite. The solution composition path is such that between D and F f_{O_2} increases along the hematite-chalcopyrite phase boundary until between F and G all hematite dissolves as pyrite forms. This interval is critical as it corresponds to a copper minimum in the rock as indicated in Figure 13. There is a

corresponding maxima in the copper content of the aqueous fluid showing that all copper initially contained in the rock has been leached out and is stored in the aqueous fluid responsible for the oxidation of the protore. The mineral assemblage formed at point G is pyrite-quartz-muscovite, or barren quartz-pyrite, representing a major transition in mineralization history from copper fixation to total leaching. At higher fluid/rock ratios, copper is again fixed as sulfides, first as bornite and eventually as covellite at the highest oxidation states.

It is significant that over the reaction path the H_2S fugacity and the corresponding $\log f_{S_2}/f_{O_2}$ first decreased up to point D and then increased from F to L (Fig. 12B). This behavior is seen in Figure 2 as a change from a positive reaction path slope to a negative slope at point F. The oxygen fugacity actually passes through a maximum value higher than the oxidizing fluid as hematite dissolves liberating oxygen into solution. It is at this maxima in the oxidation state that the barren quartz-pyrite assemblage forms during the most intense copper leaching of the protore. As seen in Figures 2 and 13, the advanced argillic assemblage dominates from this point on. The state of peroxidation is depicted in Figure 12B as points along the reaction path which are above the phase boundary surface, below which a copper-bearing sulfide is stable, i.e., py (cp) or py (bn) such that strong leaching occurs. The major interval of leaching (F-G) is accompanied by strong sericitization (muscovitization, Fig. 7A) as the reaction path moves from the orthoclase-muscovite phase boundary and approaches the triple point kaolinite-muscovite-alunite. The pH of the solution has progressively diminished from approximately 5.5 to 3.1 over the course of the reaction by hydrolysis.

TABLE 2. Modal Data for Reactant Assemblages

	Volume %	
	A (quartz, monzonite)	B (diorite)
Albite	37	64
Orthoclase	22	9
Quartz	23	7
Annite	12	15
Magnetite	2	2
Pyrite	3	
Chalcopyrite	1	1
Pyrrhotite		2
	100	100

Diorite model pyrrhotite-pyrite protore

Interaction of a dioritic protore (Table 2) with oxidizing fluids has been computed and the results are shown in Figures 14 and 12C. Overall, the mineralogic predictions and mass transfer mecha-

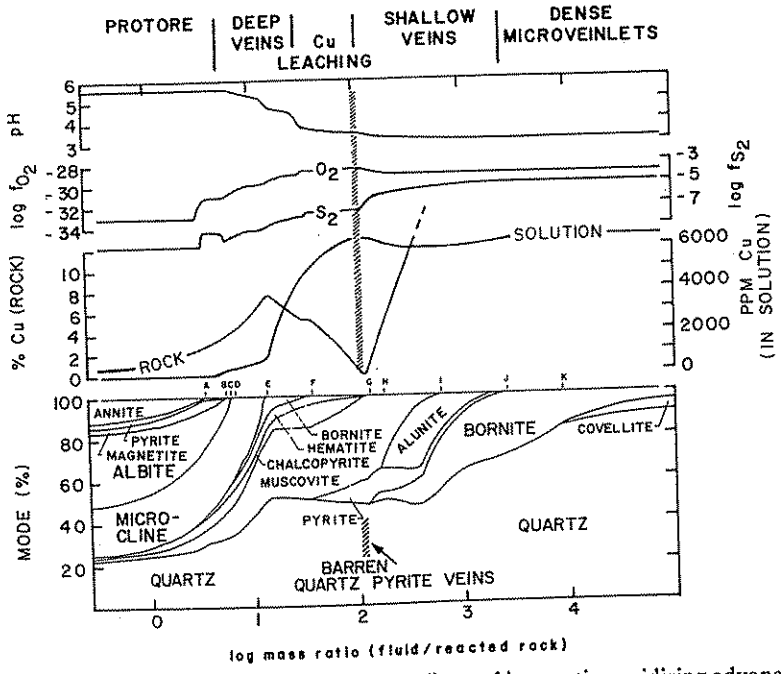

FIG. 13. Calculated mineralogical and chemical effects of interacting oxidizing advanced argillic fluids with fresh chalcopyrite-pyrite-magnetite protore at 300°C and 500 bars, the Lowell and Guilbert assemblage seen in Figures 2, 5, 7, 8, and 10. Sequence letters A through K define the reaction path shown in Figure 12B.

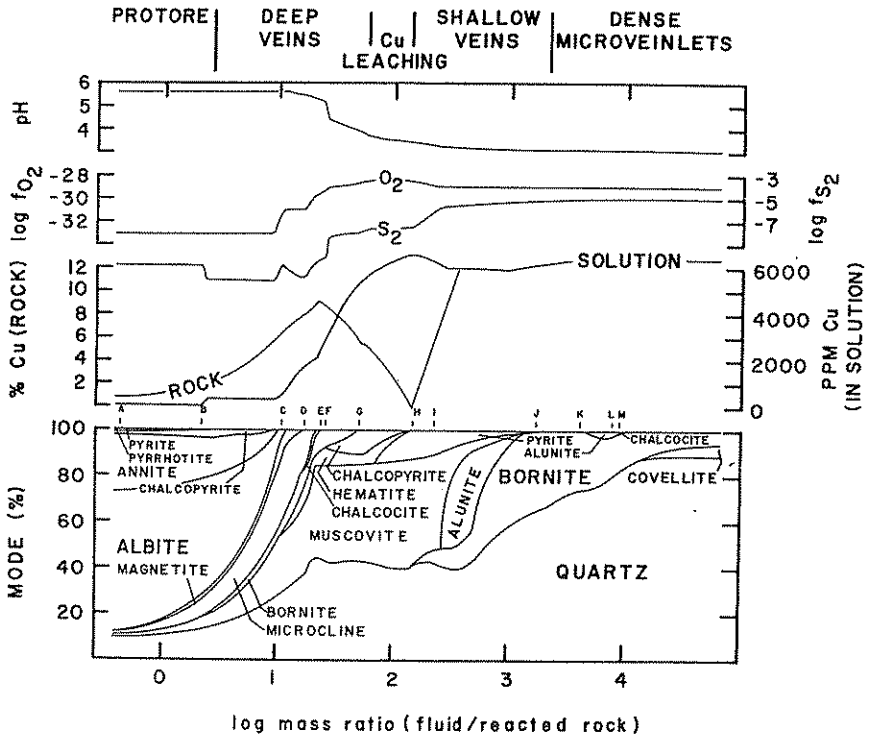

FIG. 14. Calculated mineralogical and chemical effects of oxidation of diorite protore containing chalcopyrite-pyrrhotite. Sequence letters A through M are shown in Figure 12C.

nisms including copper leaching at the barren quartz-pyrite peroxidation stage are the same as for the monzonite model even though the initial fo_2 is lower (Fig. 10). The advanced argillic alteration assemblage is also produced at high fluid/rock ratios including chalcocite-covellite assemblages.

Quartz monzonite protore without magnetite

In order to understand better the buffering effects of the protore mineral assemblages on the initial segments of the reaction paths during oxidation, interaction of a magnetite-free chalcopyrite-pyrite protore with the oxidizing fluid has been computed (Figs. 15 and 12D). The initial assemblage, as positioned along line A-B in Figure 10, is at lower oxygen fugacities than the magnetite-chalcopyrite-pyrite protore (A) shown in Figure 13.

Oxidation and sulfidation proceed in much the same manner as in the magnetite-bearing quartz monzonite protore and, although peroxidation occurs, total copper leaching does not (Fig. 12D). The copper content of the fluid and idealized rock is shown for this model as well as for the magnetite-bearing counterpart. A copper minima does occur at a fluid/rock ratio where a quartz-pyrite assemblage is predicted, but the mineral assemblage contains approximately 2 percent copper instead of zero as in Figure 13. This copper retention is the result of the solution composition, which never rises above the phase boundary py (cp) or py (bn) into the pyrite field, which is above the thermodynamic stability of a copper-iron sulfide (Fig. 12D). Consequently, a smooth transition occurs from the pyrite-chalcopyrite assemblage into one with pyrite-bornite. In contrast the models previously discussed involved a total destruction of the chalcopyrite before bornite saturation was attained.

Interpretation of Results

By utilizing the computed fluid/rock ratio as the independent variable in interpreting the oxidation process, many mineralogic and chemical effects are thermodynamically predicted which confirm and extend conclusions based entirely upon geologic data (Brimhall, 1978, 1979). The predicted sequence of secondary sulfides is exactly like that found in nature and previously described as reaction domains. The mechanism of hypogene leaching followed by enrichment has also been identified computationally and is related to exceptionally high oxidation-sulfidation states following hematite dissolution and is accompanied by pyrite-quartz formation during intense sericitization. At low fluid/rock ratios there is a multiplicity of

mineral phases which indicate the fluid is near equilibrium with the wall-rock protore. At higher fluid/rock ratios the number of mineral phases is drastically reduced indicating that the system has changed from a rock-dominated (fluid composition buffered by wall-rock mineral assemblages) to a fluid-dominated state. As the amount of fluid relative to a given quantity of rock increases, the wall-rock mineral buffers have been progressively destroyed permitting the state of oxidation-sulfidation to proceed unimpeded while hydrolysis occurs. An interpretation of the physical environment has been made incorporating the fluid/rock ratio, as indicated in Figures 11, 13, 14, and 15.

Geological studies at Butte have shown that the advanced argillic alteration assemblage and coexisting chalcocite-covellite veinlets are often geometrically related to horsetail structures, or zones of exceptionally high fracture (vein) density. These zones of high permeability are also interpreted to be zones of the highest fluid/rock ratio. In each of the figures these zones are defined as dense microveinlet zones. In contrast, at lower fluid/rock ratios the protores represent mineral assemblages totally unaffected by oxidizing fluids. Between these two extremes, i.e., protore and dense microveinlet assemblages corresponding to lowest and highest fluid/rock ratios, are intermediate assemblages interpreted here to represent intermediate states of fluid-rock interaction.

One such state identified in each model which corresponds to the highest oxidation state is the barren quartz-pyrite stage invariably accompanying intense copper leaching of the protore during muscovitization. On either side of this event (in Figs. 11, 13, 14, and 15) at lower and higher fluid/rock ratios are mineral assemblages differing principally in the level of associated muscovitization. Of these, the assemblage at lower fluid/rock ratios, i.e., chalcopyrite-bornite with minor K-feldspar, is interpreted to represent the deep chalcopyrite-bornite-pyrite veins of the Butte district which often contain relict orthoclase within the sericitic alteration envelopes, the so-called "S" assemblage (Meyer et al., 1968). At fluid/rock ratios higher than those of the barren quartz-pyrite stage, pyrite-bornite assemblages are thermodynamically predicted which are interpreted to represent the upper extension of the deep veins above the 2800 level where a mineralogic transition occurs to pyrite-bornite-chalcocite assemblages (Meyer et al., 1968; Brimhall, 1979). This transition is accompanied by intense seriticization and total orthoclase destruction within the sericitic halo. These intervals are interpreted to correspond to deep veins and shallow veins as shown in Figures

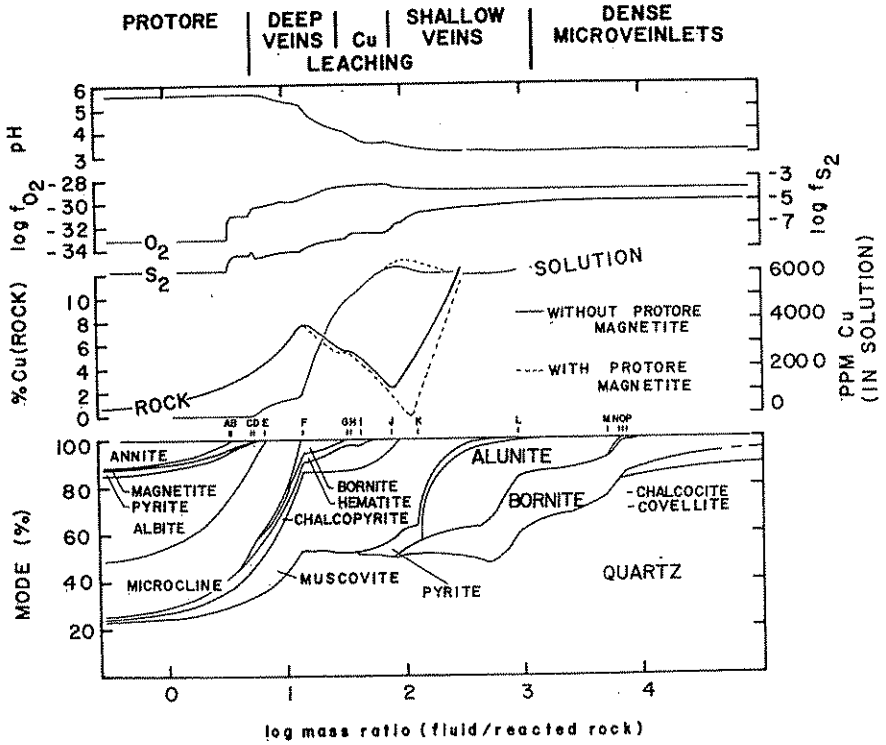

FIG. 15. Calculated mineralogical and chemical effects of oxidizing a magnetite-poor chalcopyrite-pyrite protore. Sequence letters A through P are shown in Figure 12D.

11, 13, 14, and 15. It is also possible, though unlikely, that the transition in sulfide mineralogy is induced by a temperature gradient. In all probability, the transition is most likely due to a small temperature gradient upward and to the effects of increased near-surface fracture density causing higher fluid/rock ratios.

The calculations indicate that copper redistribution between rock protore mineral assemblages and oxidizing aqueous fluids is a direct thermodynamic consequence of progressive fluid and rock interaction. These results of theoretical calculations coupled with existing knowledge of ore-forming mechanisms discovered lithologically may be generalized and may be helpful for improving the existing models of porphyry copper formation. In addition, the principles and chemical mechanisms of ore deposition may be of practical application for mineral exploration in the porphyry copper environment.

Model of Ore Deposition at Butte

The base metal ore deposit at Butte, like many porphyry copper deposits, is characterized by a complex multistage character recognized principally by cross cutting structural relationships of veins and intrusive contacts, and by radiometric dating. The first deposition of significant copper sulfides occurs within the confines of a hydrofractured volume of wall rock in and around the host pluton or dike system responsible for thermal convection of magmatically heated aqueous hydrothermal fluids. Early fracture-controlled disseminated sulfides are precipitated at high temperatures (600°–700°C) with associated potassium-silicate alteration assemblages including biotite, orthoclase, anhydrite, quartz, magnetite, muscovite, andalusite, and pyrite. Related to these early sulfides (chalcopyrite, pyrite) are disseminated sulfides in breccia zones composed of rock fragments in an orthoclase-quartz-biotite matrix. Often these early biotitic breccias (Brimhall, 1977) are geometrically related to quartz porphyry dikes and may represent water-saturated caps advancing upward ahead of arising silicate magma columns. Dense hydrofracture networks of biotitic veinlets can be found emanating from larger biotitic breccia zones, indicating that hydrothermal fluids related to crystallizing magma were also responsible for local fracture generation and copper introduction (Brimhall, 1977). A systematic evolution in early vein types and associated alteration assemblages occurs from early biotite to later quartz- and alkali feldspar-rich assemblages (Brimhall, 1977). Base metal deposition also shows a major transition from early copper sulfides to later molybdenite precipitated with little megascopically visible wall-rock alteration except for biotitization of wall-rock hornblende. Metal grades rarely exceed 0.6 to 0.7 percent copper and 0.07 percent Mo at this protore stage. It is possible that the transition from K-silicate copper-bearing assemblages to quartz-molybdenite assemblages represents a major change in the pressure regime during mineralization from early lithostatic to hydrostatic as in the El Salvador district (Gustafson and Hunt, 1975) or may simply be the result of cooling of the protore.

Transition from an early closed subsurface hydrothermal system to one in which fluid communication takes place with the surface appears to be critical in determining the ultimate distribution of ore. In many instances influx of meteoric water into a single magmatic-hydrothermal system followed by thermal collapse has produced concentric mineralization and alteration zones surrounded by a pyritic fringe. In contrast, deposits lacking a late-stage meteoric water overprint may show only the primary zonation development during early high-temperature events including a peripheral propylitic alteration zone.

Porphyry copper deposits with a more complex history, e.g., Butte, may result from multiple intrusions which may be responsible for late-stage fluid circulation geometrically related not to the expired early heat source but instead to these later thermal anomalies. The nature of the resultant hypogene modifications of the protore has been shown to be mainly a function of the amount of hydrothermal fluids circulating through the mineralized wall rock. In certain instances late-stage high-level intrusives, e.g., the Modoc porphyries of the Butte district, may be emplaced at a time when rapid erosion and dense near-surface fracturing involved enormous quantities of meteoric water. In these extreme cases deep hypogene oxidation occurs to an extent far in excess of that necessary to produce the effects of copper redistribution during phyllic alteration while a single early porphyry heat source decays. Thus, a complete spectrum of mineral assemblages and associated metal grades occurs. At the lowest fluid/rock ratios, deep chalcopyrite-bornite veins may form which may be destroyed by hypogene leaching if fluid circulation continues. At low fluid/rock ratios the protore mineral assemblage dominates the fluid composition. Consequently these chalcopyrite-bornite veins should occur mainly within the protore mass. At intermediate fluid/rock ratios, however, total copper extraction occurs from both relict protore and secondary vein mineralization as the state of oxidation of the fluid reaches a maximum and all protore oxygen fugacity buffer

assemblages are destroyed. At this critical fluid/rock ratio beyond which the protore exerts little influence on the fluid composition, barren quartz-pyrite veins form during intense sericitization. At higher fluid/rock ratios copper is again fixed in the vein structures as bornite-pyrite assemblages geometrically above the protore followed by high-grade chalcocite-covellite assemblages accompanied by the advanced argillic alteration assemblages. This end stage is expected only in areas of highest permeability and fracture density where prolonged fluid circulation causes the fluid/rock ratio to proceed to maximum values. In all likelihood, these conditions are met only in close proximity to the heat source responsible for fluid circulation.

While much of the systematic evolution in hypogene and supergene processes is essentially prescribed by local initial states, e.g., wall-rock and intrusive compositions, certain critical events are necessary for the attainment of economically important end-stage mineralization and alteration as in the Butte district. These events add individuality to each porphyry deposit and include the timing and position of high-level intrusives and fracture systems—both critical factors in determining whether or not meteoric water becomes involved in large quantities. These special circumstances greatly enhance the material exchange between migrating hydrothermal fluids and mineralized wall rock. The progressive equilibration during successive thermal perturbations may go to uncommon extremes and are manifest in the mineralogical diversity and unusual copper abundance in large volumes of wall rock.

Speculative Implications for Mineral Exploration

It must be conceded that on the basis of the lithologic data and the thermodynamic computations of this study that the Butte protore was a necessary but not sufficient condition for copper vein and horsetail formation. As discussed earlier, certain special circumstances are necessary to drive fluid circulation to extreme limits of fluid/rock ratio, e.g., young high-level intrusives and related dense fracture networks. It is therefore reasonable, upon extending an analysis of this system, that many porphyry copper systems should consist mainly of a K-silicate stage with concentrically zoned peripheral alteration facies, which never evolved to end-meteoric water stages. Conversely, there is reason to expect that surficial vein copper and possibly precious metal deposits of substantial tonnage may be underlain by disseminated sulfide protores of considerable size, which at least in part may have undergone deep hypogene modification including the formation of a strongly sericitized barren quartz-pyrite relict. This modification might conceivably occur in one of several ways, the first of which would be affected by relatively late, though cogenetic, calc-alkaline intrusives and related fracture systems within a district. In addition, regions characterized by a volcano-tectonic transition, e.g., the Basin and Range province (Lipman et al., 1972; Christiansen and Lipman, 1972), might contain very old protores which only recently have been exposed in post-Miocene time to deeply circulating meteoric water controlled by extensive listric faulting and bimodal plutonism.

The hypogene oxidation process described, related to either synchronous or diachronous plutonism, involves intimate chemical exchange between hydrothermal fluids and surrounding wall rocks, thus causing a diversity of mineralogical effects of potential use in mineral exploration. Chemical reactions resulting in the simultaneous growth of secondary mineral assemblages in both wall rock and veins may ultimately reduce the permeability of the rock to the point where fluid circulation ceases altogether. This self-sealing mechanism may be responsible for the preservation of diverse reaction stages spanning the full spectrum of hypogene leaching and enrichment phenomena in a given deposit. The relict mineral assemblages produced by this permeability-reduction mechanism offer a complete record of the progressive chemical evolution of a magmatic-hydrothermal system documenting in a three-dimensional framework the fluid/rock ratio at the time of cessation of fluid circulation.

It is evident from this study that there are certain fluid/rock ratios favorable for copper fixation, i.e., in high-grade veins at low ratios and in dense microfractured volumes of considerable size at extremely high fluid/rock ratios. At intermediate ratios total copper leaching occurs creating potentially large volumes of barren rock and districts where all copper has left the system. By analyzing the geometric distribution of available mineral assemblages in a district with respect to likely heat sources for fluid motion, it should be possible to identify zones within a deposit where multistage processes should have strongly enhanced the total copper grade of the rock. Similarly, net leached zones should be expected and in all probability will contain an abundance of barren quartz-pyrite veins in strongly sericitized wall rock stripped of its protore copper content.

Acknowledgments

The research described in this paper has been supported by the California Institute of Mining

and Mineral Resources at the University of California, Berkeley, and NSF Grant No. EAR-7911342. It is a pleasure to acknowledge the encouragement and numerous helpful suggestions of P. Bethke, J. J. Hemley, and H. C. Helgeson. Stimulating discussions with C. Meyer, U. Petersen, M. Ghiorso, G. C. Flowers, K. Jackson, and E-an Zen were also of great help in this research effort. T. Wolery deserves special recognition for providing computer programs and very willing technical assistance. Photography was expertly performed by D. Maskell and J. Hampel, and the manuscript typed by Debbie Aoki and Stepha Genelza. Drafting was done in part by M. Lee; the bulk, however, was done by D. Cave who also cheerfully helped to carry out computer work and data compilation.

DEPARTMENT OF GEOLOGY AND GEOPHYSICS
UNIVERSITY OF CALIFORNIA, BERKELEY
BERKELEY, CALIFORNIA 94720
August 29, December 17, 1979

REFERENCES

Anderson, C. A., 1955, Oxidation of copper sulfides and secondary sulfide enrichment: ECON. GEOL. FIFTIETH ANN. VOL., p. 324–340.

Barton, P. B., Jr., 1970, Sulfide petrology: Mineralog. Soc. America Spec. Paper 3, p. 187–198.

Brimhall, G. H., Jr., 1977, Early fracture-controlled disseminated mineralization at Butte, Montana: ECON. GEOL., v. 72, p. 37–59.

—— 1978, Mechanisms of vein formation at Butte, Montana: element recycling by hypogene leaching and enrichment of low-grade K-silicate protore [abs.]: ECON. GEOL., v. 73, p. 1389.

—— 1979, Lithologic determination of mass transfer mechanisms of multiple-stage porphyry copper mineralization at Butte, Montana; vein formation by hypogene leaching and enrichment of potassium-silicate protore: ECON. GEOL., v. 74, p. 556–589.

Burnham, C. W., 1967, Hydrothermal fluids at the magmatic stage, *in* Barnes, H. L., ed., Geochemistry of hydrothermal ore deposits: New York, Holt, Rinehart, and Winston, Inc., p. 34–76.

Christiansen, R. L., and Lipman, P. W., 1972, Cenozoic volcanism and plate tectonic evolution of the western United States. II. Late Cenozoic: Royal Soc. [London] Philos. Trans., v. 271, sec. A, p. 249–284.

Creasey, S. C., 1959, Some phase relations in the hydrothermally altered rocks of porphyry copper deposits: ECON. GEOL., v. 54, p. 351–373.

Einaudi, M. T., 1977, Environment of ore deposition at Cerro de Pasco, Peru: ECON. GEOL., v. 72, p. 893–924.

Graton, L. C., and Bowditch, S., 1936, Alkaline and acid solutions in hypogene zoning at Cerro de Pasco: ECON. GEOL., v. 31, p. 651–698.

Gustafson, L. B., and Hunt, J. P., 1975, The porphyry copper deposit at El Salvador, Chile: ECON. GEOL., v. 70, p. 857–912.

Helgeson, H. C., 1968, Evaluation of irreversible reactions in geochemical processes involving minerals and aqueous solutions—I. Thermodynamic relations: Geochim. et Cosmochim. Acta, v. 32, p. 853–877.

—— 1969, Thermodynamics of hydrothermal systems at elevated temperatures and pressures: Am. Jour. Sci., v. 267, p. 729–804.

—— 1970, A chemical and thermodynamic model of ore deposition in hydrothermal systems: Mineralog. Soc. America Spec. Paper 3, p. 155–186.

—— 1971, Kinetics of mass transfer among silicates and aqueous solutions: Geochim. et Cosmochim. Acta, v. 35, p. 421–469.

Helgeson, H. C., and Kirkham, D. H., 1974, Theoretical prediction of the thermodynamic behavior and aqueous electrolytes at high pressures and temperatures: I. Summary of the thermodynamic/electrostatic properties of the solvent: Am. Jour. Sci., v. 274, p. 1089–1198.

Helgeson, H. C., Garrels, R. M., and MacKenzie, F. T., 1969, Evaluation of irreversible reactions in geochemical processes involving minerals and aqueous solutions—II. Applications: Geochim. et Cosmochim. Acta, v. 33, p. 455–481.

Helgeson, H. C., Brown, T. H., Nigrini, A., and Jones, T. A., 1970, Calculation of mass transfer in geochemical processes involving aqueous solutions: Geochim. et Cosmochim. Acta, v. 34, p. 569–592.

Helgeson, H. C., Delany, J. M., Nesbitt, H. W., and Bird, D. K., 1978, Summary and critique of the thermodynamic properties of rock-forming minerals: Am. Jour. Sci., v. 278-A, p. 1–229.

Helgeson, H. C., Kirkham, D. H., and Flowers, G. C., 1980, Theoretical prediction of the thermodynamic behavior of aqueous electrolytes at high pressures and temperatures: IV. Calculation of activity coefficients, osmotic coefficients, and apparent molal and standard and relative partial molal properties to 600°C and 5 kb: Am. Jour. Sci. (in press).

Hemley, J. J., Meyer, C., Hodgson, C. J., and Thacher, A. B., 1967, Sulfide solubilities in alteration-controlled systems: Science, v. 158, p. 1580–1582.

Hemley, J. J., Hostetler, P. B., Gude, A. J., and Mountjoy, W. T., 1969, Some stability relations of alunite: ECON. GEOL., v. 64, p. 599–612.

Holland, H. D., 1959, Some applications of thermochemical data to problems of ore deposits. I. Stability relations among the oxides, sulfides, sulfates, and carbonates of ore and gangue metals: ECON. GEOL., v. 54, p. 184–233.

—— 1965, Some applications of thermochemical data to problems of ore deposits II. Mineral assemblages and the composition of ore-forming fluids: ECON. GEOL., v. 60, p. 1101–1166.

Hollister, V. F., 1978, Geology of the porphyry copper deposits of the Western Hemisphere: New York, Am. Inst. Mining Metall. Petroleum Engineers, 219 p.

—— 1979, Porphyry copper-type deposits of the Cascades volcanic area, Washington: Minerals Sci. Eng., v. 11, p. 22–35.

Knight, J. E., 1977, A thermochemical study of alunite, enargite, luzonite, and tennantite deposits: ECON. GEOL., v. 72, p. 1321–1336.

Lacy, W. C., and Hosmer, H. L., 1956, Hydrothermal leaching in central Peru: ECON. GEOL., v. 51, p. 69–79.

Lipman, P. W., Prostka, H. J., and Christiansen, R. L., 1972, Cenozoic volcanism and plate tectonic evolution of the western United States. I. Early and Middle Cenozoic: Royal Soc. [London] Philos. Trans., v. 271, p. 217–248.

Lowell, J. D., 1974, Regional characteristics of porphyry copper deposits of the southwest: ECON. GEOL., v. 69, p. 601–617.

Lowell, J. D., and Guilbert, J. M., 1970, Lateral and vertical alteration-mineralization zoning in porphyry ore deposits: ECON. GEOL., v. 65, p. 373–408.

Meyer, C., 1965, An early potassic type of alteration at Butte, Montana: Am. Mineralogist, v. 50, p. 1717–1722.

Meyer, C., and Hemley, J. J., 1967, Wall rock alteration, *in* Barnes, H. L., ed., Geochemistry of hydrothermal ore deposits: New York, Holt, Rinehart and Winston, Inc., p. 166–235.

Meyer, C., Shea, E. P., Goddard, C. C., Jr., and staff, 1968, Ore deposits at Butte, Montana, *in* Ridge, J. D., ed., Ore deposits of the United States, 1933–1967 (Graton-Sales vol.): New York, Am. Inst. Mining Metall. Petroleum Engineers, v. 2, p. 1363–1416.

Montoya, J. W., and Hemley, J. J., 1975, Activity relations and stabilities in alkali feldspar and mica alteration reactions: ECON. GEOL., v. 70, p. 577–594.

Norton, D. L., and Knight, J., 1977, Transport phenomena in hydrothermal systems: Cooling plutons: Am. Jour. Sci., v. 277, p. 937–981.

Putman, G. W., 1972, Base metal distribution in granitic rocks: Data from the Rocky Hill and Lights Creek stocks, California: Econ. Geol., v. 67, p. 511–527.

—— 1973, Biotite-sulfide equilibria in granitic rocks: A revision: Econ. Geol., v. 68, p. 884–891.

Raymahashay, B. C., and Holland, H. D., 1969, Redox reactions accompanying hydrothermal wall rock alteration: Econ. Geol., v. 64, p. 291–305.

Sheppard, M. F., and Taylor, H. P., Jr., 1974, Hydrogen and oxygen isotope evidence for the origins of water in the Boulder batholith and Butte ore deposits, Montana: Econ. Geol., v. 69, p. 926–946.

Taylor, H. P., Jr., 1974, The application of oxygen and hydrogen isotope studies to problems of hydrothermal alteration and ore deposition: Econ. Geol., v. 69, p. 843–883.

Titley, S. R., 1978, Geologic history, hypogene features, and processes of secondary sulfide enrichment at the Plesyumi copper prospect, New Britain, Papua New Guinea: Econ. Geol., v. 73, p. 768–784.

Tso, J. L., Gilbert, M. C., and Craig, J. R., 1979, Sulfidation of synthetic biotites: Am. Mineralogist, v. 69, p. 304–316.

White, D. E., 1974, Diverse origins of hydrothermal ore fluids: Econ. Geol., v. 69, p. 954–973.

Wolery, T. J., 1979, Calculation of chemical equilibrium between aqueous solution and minerals: The EQ3/6 softwares package: Univ. California Lawrence Livermore Lab. Bull. 52658, 31 p.